The Astrophysical Journal, 792:43 (20pp), 2014 September 1 doi:10.1088/0004-637X/792/1/43

THE MAGELLANIC STREAM AND DEBRIS CLOUDS

B.-Q. For[1,4], L. Staveley-Smith[1], D. Matthews[2], and N. M. McClure-Griffiths[3]
[1] International Centre for Radio Astronomy Research, University of Western Australia, 35 Stirling Hwy, Crawley, WA 6009, Australia; biqing.for@icrar.org
[2] Centre for Materials and Surface Science, La Trobe University, Melbourne, VIC 3086, Australia
[3] CSIRO Astronomy and Space Science, Epping, NSW 1710, Australia
Received 2013 October 22; accepted 2014 June 24; published 2014 August 13

ABSTRACT

We present a study of the discrete clouds and filaments in the Magellanic Stream using a new high-resolution survey of neutral hydrogen (H I) conducted with the H75 array of the Australia Telescope Compact Array, complemented by single-dish data from the Parkes Galactic All-Sky Survey. From the individual and combined data sets, we have compiled a catalog of 251 clouds and listed their basic parameters, including a morphological description useful for identifying cloud interactions. We find an unexpectedly large number of head–tail clouds in the region. The implication for the formation mechanism and evolution is discussed. The filaments appear to originate entirely from the Small Magellanic Cloud and extend into the northern end of the Magellanic Bridge.

Key words: ISM: kinematics and dynamics – Magellanic Clouds – radio lines: ISM

Online-only material: color figures, machine-readable table

1. INTRODUCTION

The Magellanic Clouds (MCs) are the closest extragalactic neighbors to our Galaxy. Their gaseous component was discovered in atomic hydrogen as a coherent stream originating from the MCs, namely the Magellanic Stream (MS; Wannier & Wrixon 1972; Mathewson et al. 1974) and Leading Arm (LA; Putman et al. 1998). The MS is trailing the MCs and has been subdivided into six main concentrations (MS I–VI) (Mathewson et al. 1974). Although this subdivision is an oversimplification, it is widely used to describe different regions along the stream in the literature.

Recent, detailed studies in the outskirts of the MS have made new discoveries. Several new filaments parallel with the MS (Westmeier & Koribalski 2008) and extended near its northern tip (Nidever et al. 2010) have been found. These suggest that the MS and LA now span a total of $\sim 200^\circ$ in length across the sky and are $\sim 30^\circ$ wide at their widest point. The LA, a counterpart of the MS, is leading the H I gas stream and is morphologically very different from the MS. It is dominated by three distinctive high-velocity cloud (HVC) complexes (LA I–III; Putman et al. 1998; Brüns et al. 2005), and LA IV, which is either formed by a population of HVCs as defined by For et al. (2013; hereafter FSM13) or as a single HVC complex defined by Venzmer et al. (2012).

The formation and origin of the MS and LA are still under debate. However, there are two well-studied physical mechanisms that may be the cause for their formation: ram pressure stripping of gas from the MCs due to interaction with the Galactic halo (e.g., Moore & Davis 1994; Mastropietro et al. 2005), or tidal interaction between the Milky Way and the MCs (e.g., Gardiner & Noguchi 1996; Connors et al. 2006). Both scenarios were modeled and both required orbits to reproduce the global observed H I column density and velocity distribution of the MS and LA. High-precision *Hubble Space Telescope* (*HST*) proper motion measurements of the MCs (Kallivayalil et al. 2006a, 2006b, 2013) favor either an unbound orbit for the MCs with a first passage scenario (Besla et al. 2007) or an eccentric long period orbit (Shattow & Loeb 2009). The new scenarios proposed based on the *HST* proper motion measurements have drawn controversy as tidal and ram pressure stripping require the MCs to be relatively close to the Milky Way for a long interaction time (multiple orbits). However, recent simulations have shown that the tidal force of the Large Magellanic Cloud (LMC), acting on the Small Magellanic Cloud (SMC) alone, can create the MS and LA before the MCs were accreted by the Milky Way in the first passage scenario (Besla et al. 2012; Diaz & Bekki 2012). Simulations with a bound orbit and extra drag have also successfully reproduced the observed bifurcation of the MS and remain consistent with the second epoch proper motion data (Diaz & Bekki 2011). A blowout hypothesis has been proposed by Nidever et al. (2008). They suggest that the supergiant shells in the southeast H I overdensity region of the LMC are blown out to larger radii where ram pressure and/or tidal forces can more easily strip the gas into the MS and LA. Connections between gas in the LMC and the Bridge, Stream, and LA have previously been pointed out by other authors (McGee & Newton 1986; Putman et al. 1998, 2003; Staveley-Smith et al. 2003), though not as the main source of gas feeding the stream.

An observational approach to trace the origin of the MS and LA uses metallicity measurements as an indicator. Early studies of metallicity measurements from the *HST* spectra of background sources toward the MS and LA II constrain their origin to the MCs ($Z = 0.2$–0.4 solar; Lu et al. 1994, 1998; Gibson et al. 2000). Subsequent studies with the *HST* and/or *FUSE* spectra suggest that the MS and LA originate from the SMC (Sembach et al. 2001; Fox et al. 2010). Recent metallicity measurements based on the VLT/UVES and *HST*/COS spectra of four background active galactic nuclei strongly support a scenario in which most of the stream gas was stripped from the SMC (Fox et al. 2013). However, a subsequent study of the same series reports a much higher metallicity (S/H = 0.5 solar) in the inner Stream toward background quasar, Fairall 9 (Richter et al. 2013). The overall chemical abundances of MS toward Fairall 9 are significantly different as compared to other sightlines, suggesting that the stream has a complex enrichment history. They favor the explanation of local α-enrichment by massive stars followed by separation from the MCs before nitrogen enrichment occurred. They also state that the finding supports

[4] SIEF John Stocker Fellow.

the dual origin as identified by Nidever et al. (2008) but it is not a requirement. Nevertheless, there is still a limitation to the ability of theoretical models to reproduce the general observed LA features and complex filamentary structure of the MS. Physical properties of HVCs, such as the multiphase structures formed via hydrodynamical interactions with the hot halo, are seldom able to be considered in simulations.

Large-scale H I surveys have provided huge amounts of information for studying the gaseous structures surrounding our Milky Way. The most notable surveys are the H I Parkes All-Sky Survey (HIPASS; Barnes et al. 2001), the Leiden–Argentine–Bonn all-sky H I survey (LAB; Kalberla et al. 2005) and the Galactic All-Sky Survey (GASS; McClure-Griffiths et al. 2009) in the Southern hemisphere. HIPASS is an extragalactic survey with a coarse velocity resolution ($\Delta v \sim 18$ km s^{-1}) but it is very sensitive and covers a large range in velocity. The data were employed to create an HVC catalog (Putman et al. 2002, hereafter P02) and to recover the extended structure of the Magellanic System (Putman et al. 2003). GASS is a Galactic survey with a much better spectral resolution ($\Delta v = 1$ km s^{-1}) and is far more suitable for studying the gaseous feature of the Magellanic System. LAB also has good spectral resolution ($\Delta v \sim 1.3$ km s^{-1}) but it has less angular resolution than GASS. The LAB data were employed by Nidever et al. (2008) for their study on the Magellanic System. Other smaller scale studies for the Magellanic System or subregions include, for example, the narrow-band Parkes H I survey (Brüns et al. 2005), H I Galactic studies with Arecibo *L*-band Feed Array (GALFA-HI; Stanimirović et al. 2008), and a Green Bank Telescope survey (Nidever et al. 2010).

In this paper, we study the overall morphology of the MS using interferometric and single dish data, the general distribution, the physical properties, and the morphological properties of its HVCs. The aims are (1) to understand the formation and origin of the MS, (2) to investigate the effect of interaction with the Galactic halo, and (3) to provide constraints for simulations based on the observed properties. In Sections 2 and 3, we describe the observations and the procedures for source finding. We present the catalog and cloud properties in Sections 4 and 5. Cloud morphology, kinematic distribution, and interpretation of the distributions are presented in Section 6. We discuss the implications of the HVCs on the formation of the MS by comparing the observed properties with theoretical models in Section 7. A summary and conclusions are given in Section 8.

2. OBSERVATIONS AND DATA

A detailed description of the observing strategy and data reduction for the ATCA high-resolution MS survey is given in D. Matthews et al. (2014, in preparation). Descriptions of GASS are given by McClure-Griffiths et al. (2009) and Kalberla et al. (2010). A brief summary of the observations and characteristics of the data is given below.

The ATCA high-resolution MS survey covers a 500 deg^2 field of the MS using the H75 configuration of the ATCA. MS I to MS IV, part of the SMC, and the Interface Region (IFR) are covered in this survey. The observations were carried out over a period from 2005 to 2006, which resulted in ∼180 hr of total observing time. The entire area was divided into 33 regions with 154 pointing centers per region, resulting in 5082 pointing centers. Each pointing center was separated by 20′, arranged in a hexagonal grid, observed for 20 s, and revisited six times during an average of 10 hours of observation. The resulting ATCA data have an angular resolution of 413″ × 330″, a brightness sensitivity of 210 mK and a velocity resolution of 1.65 km s^{-1} after Hanning smoothing. The survey covers the local standard of rest velocity (V_{LSR}) between −315 and +393 km s^{-1}.

GASS is an H I survey of the entire sky south of declination +1° using the 20 cm multibeam receiver on the Parkes radio telescope. This survey covers V_{LSR} between −400 and +500 km s^{-1}. The second data release[5] employed in this study has been corrected for stray radiation and radio frequency interference, has a channel width of 0.82 km s^{-1}, a spectral resolution of 1 km s^{-1}, a brightness temperature (T_B) rms sensitivity of 57 mK, and an angular resolution of 16′.

The reduced ATCA images are grouped into 11 data cubes (see D. Matthews et al. 2014, in preparation for the boundary of each data cube). To obtain the large-scale structure information missing from the interferometric data, D. Matthews et al. (2014, in preparation) combined the ATCA data with the GASS data, hereafter H75GASS. The GASS data were matched to the angular dimensions of each ATCA data cube prior to merging, and were merged in the image domain as detailed by D. Matthews et al. (2014, in preparation). The merged data have an average T_B sensitivity of 250 mK and are in equatorial coordinates.

To precisely and conveniently describe the position of various gaseous features along the MS, many have used a Magellanic coordinate system. For example, Wakker (2001) defined the north pole of the Magellanic coordinate system as Galactic longitude (l) 180° and latitude (b) 0°. Its equator passes through the Galactic equator at $l = 90°$ and $b = 270°$ and passes through the south Galactic pole (SGP). However, this definition does not place the equator exactly along the MS. A new coordinate system, the MS coordinate, has since been introduced by Nidever et al. (2008) to better represent the projection of the MS along the equator. This new coordinate system defines $L_{MS} = 0°$ at the center of the LMC, i.e., $(l, b) = 280.°47, -32.°75$ (van der Marel et al. 2002), and the pole at $(l, b) = 188.°5, -7.°5$. The L_{MS} decreases in value toward the tip of the MS and increases in value toward the LA. We adopt this coordinate system for the rest of the paper.

3. SOURCE FINDING

3.1. Preparation

We converted the H75GASS data cubes into Galactic coordinates, with each covering a different range of velocities. To minimize the size of the data cubes, we created 12 subcubes covering the velocity range that contains obvious features of the MS. Any feature in the range of -30 km s^{-1} $< V_{LSR} <$ +18 km s^{-1} is indistinguishable from the strong Galactic H I emission and hence was excluded. Mild contamination from the Galactic H I emission occurs at $-40 \lesssim V_{LSR} \lesssim -30$ km s^{-1} and $+18 \lesssim V_{LSR} \lesssim +30$ km s^{-1}, which predominantly affects region −55° to −40° in L_{ms}. A mosaicked cube containing features of the MS at positive and negative LSR velocity was also created. A summary of velocity ranges for the original cubes and created subcubes is given in Table 1 (see D. Matthews et al. 2014, in preparation for the boundary of each data cube).

For the GASS data alone, we also extracted data cubes that covered a similar region and velocity range, giving a total of four data cubes (negative velocity and positive velocity for both H75GASS and GASS) for source finding. Integrated H I column density maps of the mosaicked H75GASS and GASS data are shown in zenithal equal area projection in Figures 1 and 2.

[5] http://www.astro.uni-bonn.de/hisurvey/gass

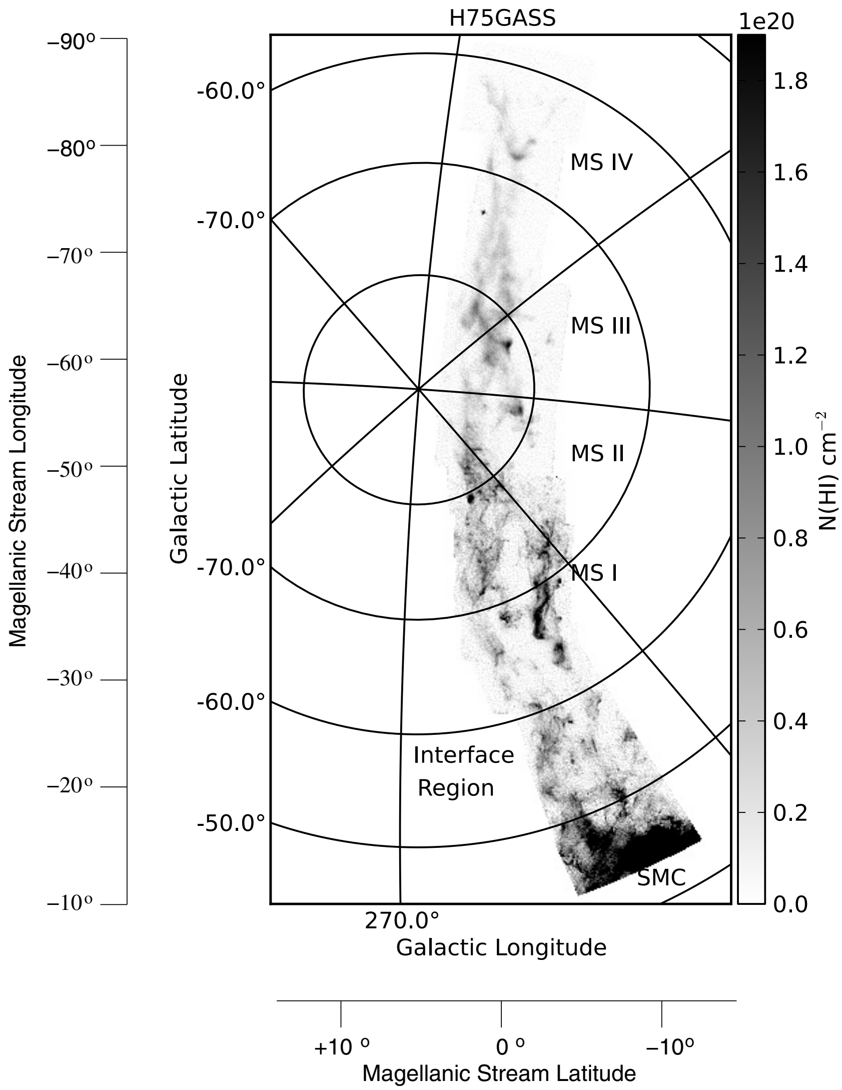

Figure 1. Integrated H I column density map of H75GASS for positive and negative velocities. The H I column density ranges from 0 to 1.9×10^{20} cm^{-2}. The locations of the Small Magellanic Cloud, the Interface Region, and MS I–IV are labeled.

Table 1
The Velocity Ranges of the Original Cubes and Extracted Subcubes

Cube	Full V_{LSR} Range (km s^{-1})	Extracted V_{LSR} Range (km s^{-1})
1	−111.45 to + 382.05	+45.17 to + 279.58
2	−111.21 to + 382.28	+23.97 to + 261.65
3	−110.55 to + 382.95	+18.03 to + 214.42
4	−109.61 to + 383.89	+18.97 to + 190.58
5	−324.38 to + 330.30	+18.90 to + 227.87
		−110.30 to − 31.19
6	−323.07 to + 331.60	−201.25 to − 31.54
7	−320.97 to + 333.70	−209.04 to − 31.09
8	−318.94 to + 335.75	−249.81 to − 48.84
9	−317.83 to + 338.88	−255.28 to − 72.45
10	−315.68 to + 339.02	−259.72 to − 114.79
11	−314.30 to + 340.40	−255.05 to − 149.68

3.2. Analysis

We performed the source finding using *Duchamp*[6] version 1.2.2, a three-dimensional source finder developed by Whiting (2012). It is designed to search data cubes, merge detections, and measure basic parameters of the detected sources. It also implements optional noise reduction routines, such as the wavelet reconstruction and spatial or spectral smoothing, to enhance the detectability of fainter sources.

Each of the input cubes was reconstructed with *à trous* wavelets to remove random noise prior to the search. A fixed threshold was specified for each run, and various thresholds were tested for each input cube to find the best source finding parameters. Sources were detected only if they extended across a minimum of 10 spatial pixels and ∼5 km s^{-1} in velocity space (i.e., five and three velocity channels for GASS and H75GASS, respectively). Subsequently, the detected sources were compared to earlier detections and either merged with neighboring sources or added to the list as a single source.

Despite the application of the noise reduction technique, diffuse emission was better detected with the GASS data alone. Thus, we decided to use the H75GASS and GASS data independently to detect compact and diffuse sources, respectively. A fixed threshold of ∼2σ above the background noise (57 mK) was employed for GASS positive and negative V_{LSR} cubes. We used fixed thresholds of ∼3σ above the

6 Available at http://www.atnf.csiro.au/computing/software/duchamp/

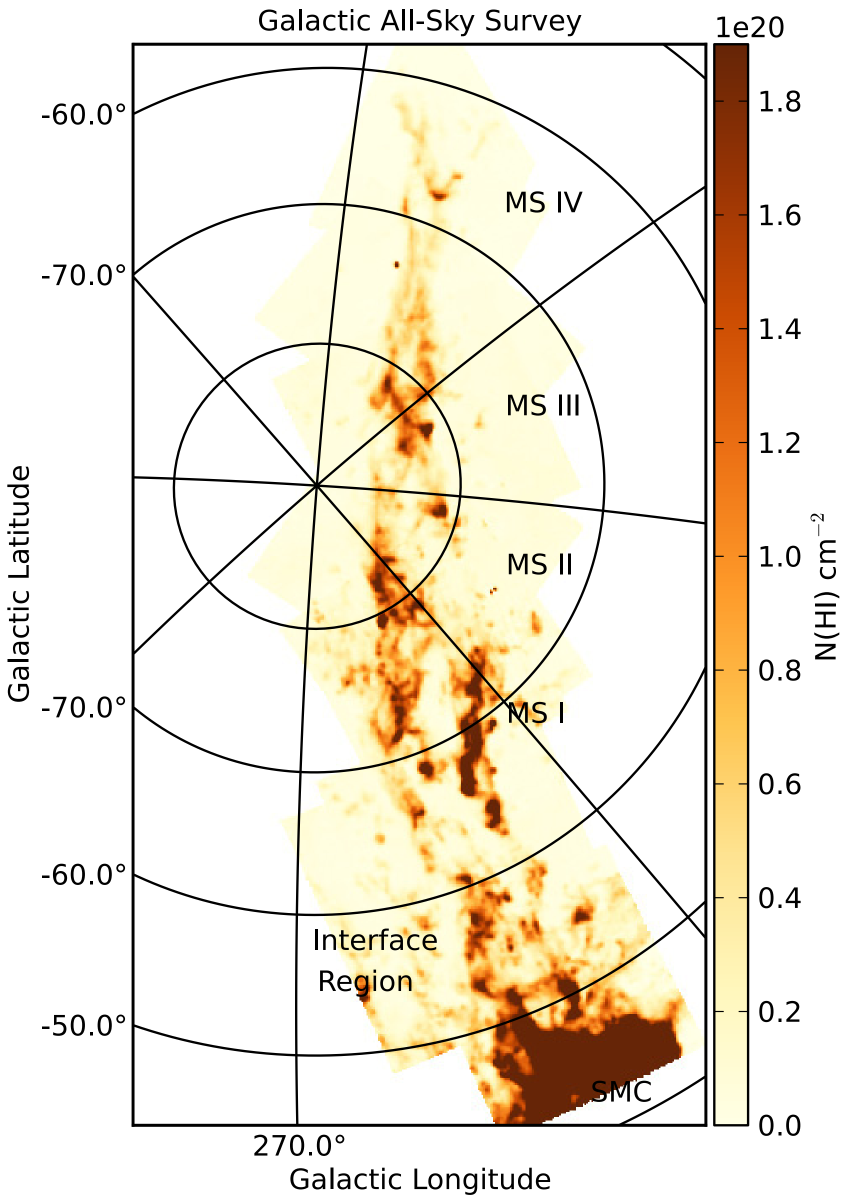

Figure 2. Same as Figure 1, but for the GASS data only. A slightly larger region than H75GASS is used in this study. A different color scheme is used to distinguish the two data sets.

(A color version of this figure is available in the online journal.)

background noise (250 mK) for the H75GASS negative and positive $V_{\rm LSR}$ cubes.

4. CATALOG

A compilation of sources with basic parameters is presented in Table 2. The catalog includes the following entries: the source identification number in Column 1; the designation with a prefix of HVC for high-velocity clouds and GLX for galaxies followed by the l, b, and central $V_{\rm LSR}$ fitted with a single Gaussian component in Column 2; MS longitude ($L_{\rm MS}$) and MS latitude ($B_{\rm MS}$) in Columns 3 and 4; central $V_{\rm LSR}$ in Column 5; the central velocity in the galactic standard of rest reference frame ($V_{\rm GSR}$), defined by $V_{\rm GSR} = 220 \cos b \sin l + V_{\rm LSR}$; the velocity in the Local Group standard of rest reference frame ($V_{\rm LGSR}$), defined by $V_{\rm LGSR} = V_{\rm GSR} - 62 \cos l \cos b + 40 \sin l \cos b - 35 \sin b$ (Braun & Burton 1999) in Columns 6 and 7; velocity FWHM, measured at 50% of peak flux in Column 8; integrated flux, peak $T_{\rm B}$, and peak H I column density ($N_{\rm H\,I}$) in Columns 9–11; semi-major axis, semi-minor axis, and position angle in Columns 12–14; warning flag, morphological classification, data origin, and comment in Columns 15–18.

We detected a total of 574 sources in our initial search. In the case of the same source being detected in both GASS and H75GASS cubes, we examined the spectrum and adopted the parameters of the source with higher spectral signal-to-noise ratio. We also examined individual spectra and the data cube in order to eliminate false detections. Such detections are caused by background artifacts and noise peaks, which generally have a narrow line width. The positions of all final sources were examined using the NASA/IPAC Extragalactic Database to identify galaxies. Seventy-five sources overlap with the Galactic emission channels and/or lie at the spatial edge of the image. These sources are included in the catalog but their physical parameters are omitted. The final catalog includes a total of 251 HVCs and two galaxies (NGC 300 and WLM). NGC 55 and

Table 2
Catalog of Detected Sources in the Region of the Magellanic Stream

ID	Designation	L_{MS}	B_{MS}	V_{LSR}	V_{GSR}	V_{LGSR}	FWHM	F_{int}[a]	T_B	N_{HI}	Semi-major	Semi-minor	PA	Flag[b]	Classification[c]	Data[d]	Comment
	($l \pm b + V_{LSR}$)	(°)	(°)	(km s^{-1})	(km s^{-1})	(km s^{-1})	(km s^{-1})	(Jy km s^{-1})	(K)	(10^{19} cm^{-2})	(°)	(°)	(°)				
(1)	(2)	(3)	(4)	(5)	(6)	(7)	(8)	(9)	(10)	(11)	(12)	(13)	(14)	(15)	(16)	(17)	(18)
24	HVC+347.9−83.8−192	−55.0	+01.7	···	···	···	···	···	···	···	···	···	···	SR	···	G	
25	HVC+072.3−70.0−191	−75.0	−01.5	−191.0	−119.3	−079.8	21.1	12.2	1.32	2.84	0.4	0.2	17	···	IC	H	
26	HVC+064.3−61.3−191	−80.8	−08.8	−190.6	−095.5	−060.4	21.0	3.5	0.23	0.36	0.2	0.2	45	···	S	G	
27	HVC+019.8−78.1−189	−59.5	−04.2	−189.4	−174.0	−149.0	5.4	1.5	1.36	1.18	0.1	0.1	−67	···	S	H	
28	HVC+079.6−78.5−188	−68.1	+03.7	−187.9	−144.5	−104.6	13.7	5.2	0.27	0.37	0.3	0.3	−76	···	pHT	G	
29	HVC+069.2−72.8−180	−72.1	−01.1	−180.4	−119.6	−081.6	45.0	27.1	1.40	3.95	0.8	0.3	−15	···	IC	H	
30	HVC+066.3−69.6−180	−74.3	−03.5	−180.3	−110.1	−073.2	22.5	9.2	1.57	3.52	0.1	0.1	78	···	:HT	H	

Notes.
[a] Corrected F_{int}.
[b] SR: the detection lies at the edge of the spectral region; E: the detection is next to the spatial edge of the image.
[c] HT: head-tail cloud with velocity gradient; :HT: head-tail cloud without velocity gradient; S: symmetric cloud; B: bow-shock cloud; IC: irregular/complex cloud.
[d] H: H75GASS; G: GASS.

(This table is available in its entirety in a machine-readable form in the online journal. A portion is shown here for guidance regarding its form and content.)

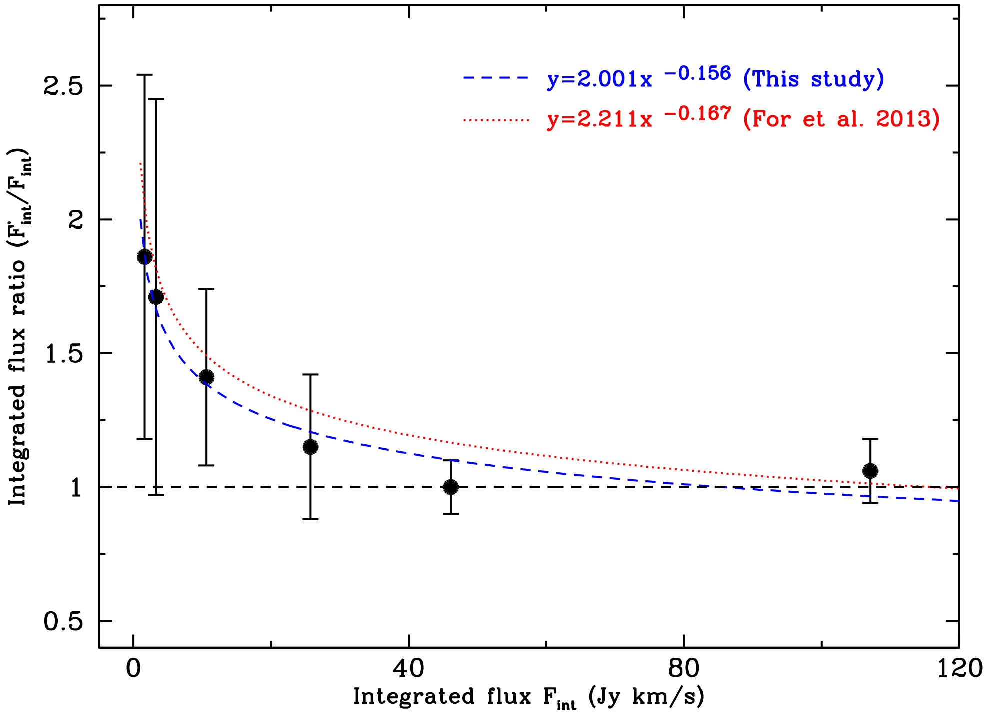

Figure 3. Ratio of true integrated flux ($F'_{\rm int}$) to integrated flux ($F_{\rm int}$) measured by *Duchamp* as a function of $F_{\rm int}$. The red-dotted and blue-dashed lines are the fitting functions derived in For et al. (2013) and this study, respectively. They represent an estimate of the correction factor to be applied to *Duchamp* fluxes.

(A color version of this figure is available in the online journal.)

NGC 7733 are positioned near the MS in the sky but are not detected because they do not fall into the field of view of the ATCA survey. NGC 55 is shown in the extracted GASS data cube, but it lies on an artifact.

The *Duchamp* software derived most of the parameters listed above except angular sizes and peak H I column density. We adopted the same approach as described in FSM13 to determine the angular sizes and peak H I column density. A two-dimensional Gaussian fitting was used to derive position angle, semi-major, and semi-minor axes. It uses the brightness centroid for the fit, though can be inaccurate for distorted sources (e.g., clouds with two bright structures). Caution should be applied when interpreting the derived position angle. The peak $N_{\rm H\,I}$ was determined by locating the brightest pixel in the integrated H I column density map of each source.

In Westmeier et al. (2012), tests were performed to evaluate the reliability of *Duchamp* for parameterizing sources. Artificial unresolved and extended H I sources were generated and tested with various parameters. They demonstrated that *Duchamp* is a powerful source finder with the capability of detecting sources down to a low signal-to-noise ratio. However, parameters such as the integrated flux ($F_{\rm int}$) measured by *Duchamp* suffer from systematic errors. The integrated flux of faint sources is underestimated by *Duchamp*. In order to correct for this systematic error, we employed the same procedures as described in FSM13 to derive the correction factor for sources in our catalog. In brief, we used the same stand-alone parameterization algorithm as employed in FSM13 to measure the integrated flux of our sources ($F'_{\rm int}$). Subsequently, the ratio of measured $F'_{\rm int}$ to $F_{\rm int}$ as a function of $F_{\rm int}$ in various bins was fitted with a polynomial. Figure 3 shows the comparison between the functions derived in this study (blue dashed line) and FSM13 (red dotted line). Both fitted functions represent the underestimation factor for a given $F_{\rm int}$ and behave similarly. Either function can be used for correcting integrated fluxes measured by *Duchamp* in future work. In this paper, we adopted the function derived from sources in this catalog.

As for derived peak $T_{\rm B}$ and peak $N_{\rm H\,I}$ measured by *Duchamp*, corrections are not necessary, but small systematic errors of the order of 5%–10% of the derived values are expected (FSM13). The velocity FWHM values measured by *Duchamp* are generally accurate (see Figure 8 of Westmeier et al. 2012).

The completeness of our catalog depends on the detection rate of *Duchamp*. Simulations to check the detection rate were performed by FSM13. Fake clouds of various input parameters were injected into the data cube at random locations and searched by *Duchamp*. They find that *Duchamp* is generally reliable for detecting clouds with narrow lines, but likely to miss clouds with faint ($T_{\rm B}$ = 0.14–1.0 K) or broad velocity lines (velocity FWHM = 16–30 km s^{-1}). The recovery rate for faint or broad velocity line clouds is 80%. We expect the same detection rate for the present catalog.

5. CLOUD PROPERTIES

In Figure 4, we show histograms of MS longitude and MS latitude in the new coordinate system, $V_{\rm GSR}$, $V_{\rm LSR}$, peak H I column density in logarithmic scale, and velocity FWHM (from top left to bottom right). Galaxies and objects with a warning flag in the catalog are excluded in these histograms. We find that the number of HVCs decreases linearly (with a determination coefficient of 0.96) from -20° to -70° in $L_{\rm MS}$. The low number of HVCs at $L_{\rm MS} = -10^\circ$ is due to the incomplete sky coverage. For $B_{\rm MS}$, the distribution is Gaussian with the peak at 0°. HVCs agglomerate in a narrow $B_{\rm MS}$ range of $\pm10^\circ$. We also find a flat distribution in $V_{\rm GSR}$ for the GASS data. Most HVCs found in the H75GASS data are distributed between 0 and 100 km s^{-1} in the GSR velocity frame. A bimodal distribution is seen in $V_{\rm LSR}$,

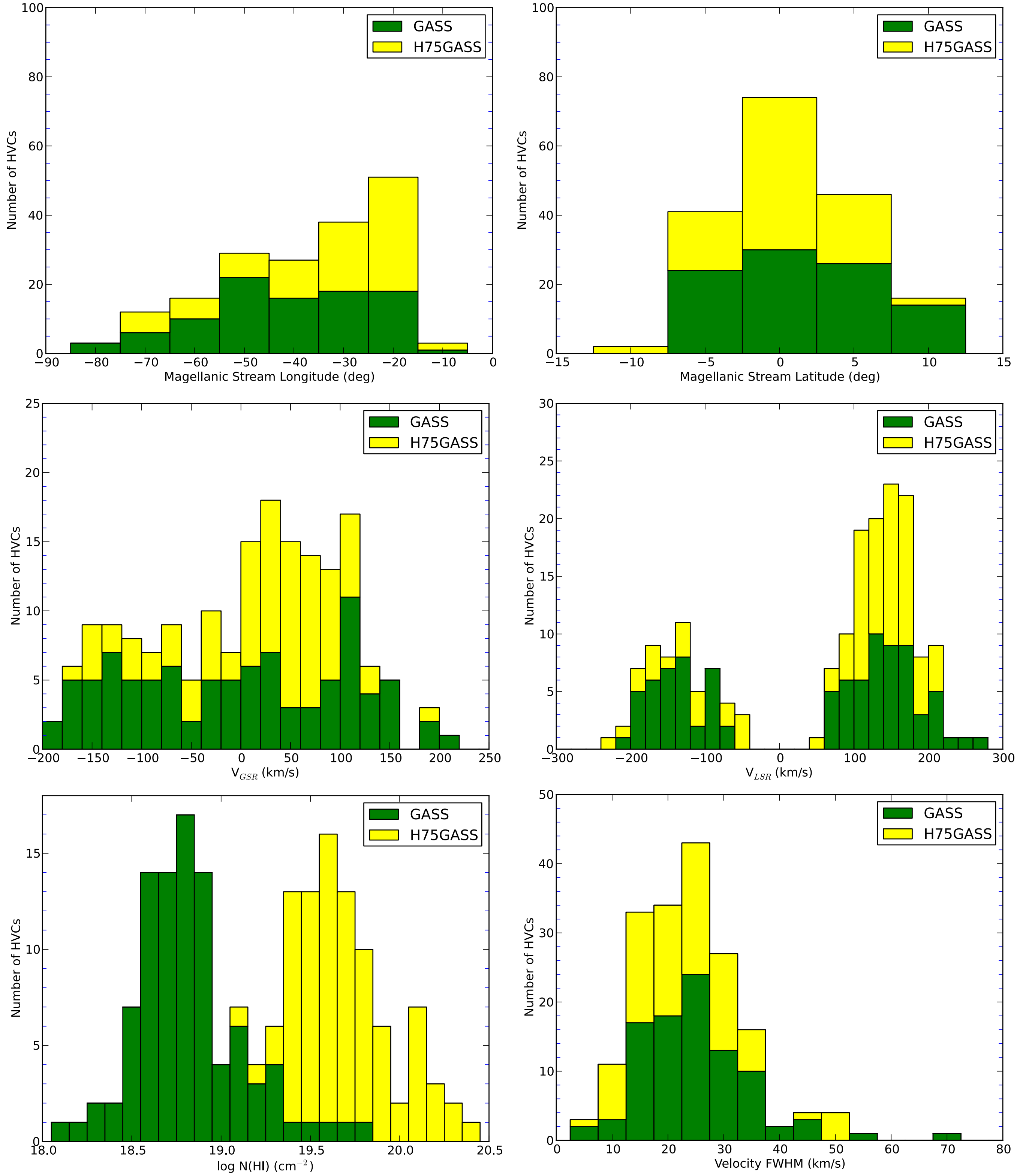

Figure 4. Stacked histograms of $L_{\rm MS}$, $B_{\rm MS}$, $V_{\rm GSR}$, $V_{\rm LSR}$, peak H I column density on a logarithm scale, and velocity FWHM of HVCs identified in GASS (green) and H75GASS (yellow), from top left to bottom right, respectively. Excluded from the plots are galaxies and 75 HVCs that either overlap with the Galactic emission channels and/or lie at the spatial edge of the image.

(A color version of this figure is available in the online journal.)

with velocity medians of −140 and +150 km s^{-1}. The lack of clouds in the negative $V_{\rm LSR}$ range is due to selection effects. The peak $N_{\rm H\,I}$ distribution is distinctly different between HVCs found in GASS and H75GASS data. Both exhibit a normal Gaussian distribution with the majority of low and high H I column density clouds being detected in GASS and H75GASS data, respectively. The lower H I column density limit in the two data sets is due to sensitivity. The gap between the histograms

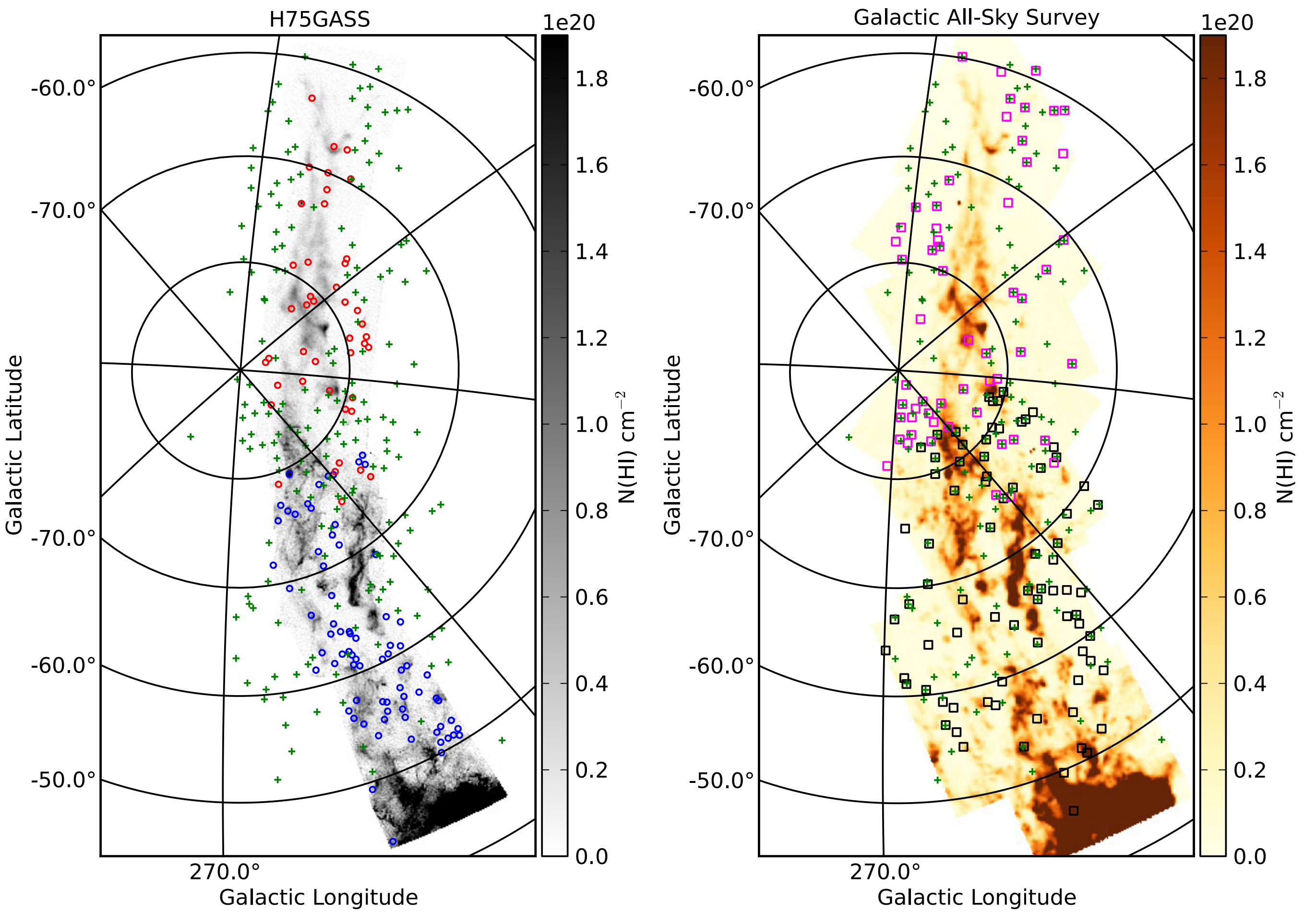

Figure 5. Left: all 118 sources detected by *Duchamp* with the H75GASS data (red and blue circles) and 183 sources detected by Putman et al. (2002) (green pluses) are overlaid onto the integrated H I column density map of H75GASS as shown in Figure 1. The blue and red circles represent *Duchamp* detections at positive and negative LSR velocities, respectively. Right: same as left panel, except 135 sources detected by *Duchamp* are from GASS data and are overlaid onto the H I column density map of GASS as shown in Figure 2. The black and magenta squares represent *Duchamp* detections at positive and negative LSR velocities, respectively. The sources from Putman et al. (2002) are within the same $V_{\rm LSR}$ range and the same region on the sky as our GASS data presented in this paper.

(A color version of this figure is available in the online journal.)

appears to be a resolution effect—peak column densities will always be higher for the higher angular resolution H75GASS data. Although not shown here, the distribution of peak $N_{\rm H\,I}$ is uniform with respect to $L_{\rm MS}$. The distribution of average column density (integrated over $B_{\rm MS}$) is also uniform in the range $L_{\rm MS} = -20^\circ$ to -70°. However, as shown in Figure 10 of Nidever et al. (2010), there is an exponential decrease thereafter. The FWHM velocity distribution suggests that clouds in this region have a median value of 25 km s^{-1} and their overall distribution is similar to that found in the LA region (FSM13), except that there are no HVCs with a velocity FWHM greater than 80 km s^{-1} in the MS region.

5.1. Comparison with the P02 Catalog

The P02 HVC catalog is based on reprocessed HIPASS data, which recovers slightly more extended emission than the original HIPASS processing (see Putman et al. 2003 for details). The search for objects was performed using a friends-of-friends cloud search algorithm (de Heij et al. 2002). The P02 catalog covers the entire right ascension range, the declination range of $\delta < +2^\circ$ and the velocity range of $-500 \leqslant V_{\rm LSR} \leqslant +500$ km s^{-1}. Since the LSR velocity range of ± 90 km s^{-1} does not exclude all the Galactic emission, an additional constraint based on the deviation velocity ($V_{\rm dev} > 60$ km s^{-1}), defined by Wakker (1991) to be the difference from a simple Galactic rotation model, was added by P02 to the selection criteria for their HVCs. They noted that the excluded objects may contain real HVCs with some having an appearance similar to the small-scale structure in the gaseous disk of the Milky Way.

In Figure 5, we show 253 sources in our catalog and 183 sources in the catalog of P02 that fall within our searched velocity and spatial volume. There are ∼71 sources identified as being the same source in two catalogs, with the majority of them detected in the GASS data (see right panel). This suggests that most of the sources detected in the H75GASS data are unique. Comparing the rates for identifying the same P02 sources between this study and FSM13, we find them to be ∼40% and ∼50%, respectively. Given the high brightness sensitivity of HIPASS as compared to GASS and H75GASS, P02 recovered many faint HVCs that were not detected in our data set (e.g., the positive MS latitudes in MS IV) in Figure 5. However, there is a lack of P02 detections in the IFR due to the nature of the reprocessed HIPASS data, in which emission is filtered out in individual channels in this region. The manner by which clouds are merged or broken up can affect overlap between the catalogs. Both GASS and H75GASS have excellent spectral resolution, which allows us to resolve HVCs with narrow lines. The high-resolution H75GASS data recover

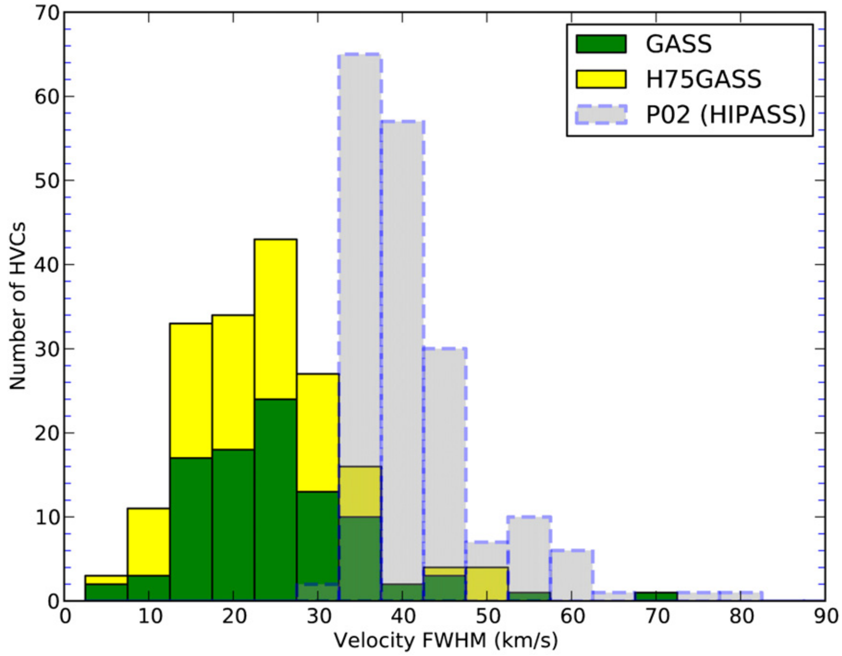

Figure 6. Histograms of velocity FWHM of HVCs in this study (green and yellow) and P02 (gray). Excluded from the plots are galaxies and 75 HVCs that either overlap with the Galactic emission channels and/or lie at the spatial edge of the image. Clouds with narrow lines are recovered in this study thanks to the higher spectral resolution of GASS and H75GASS as compared to HIPASS.

(A color version of this figure is available in the online journal.)

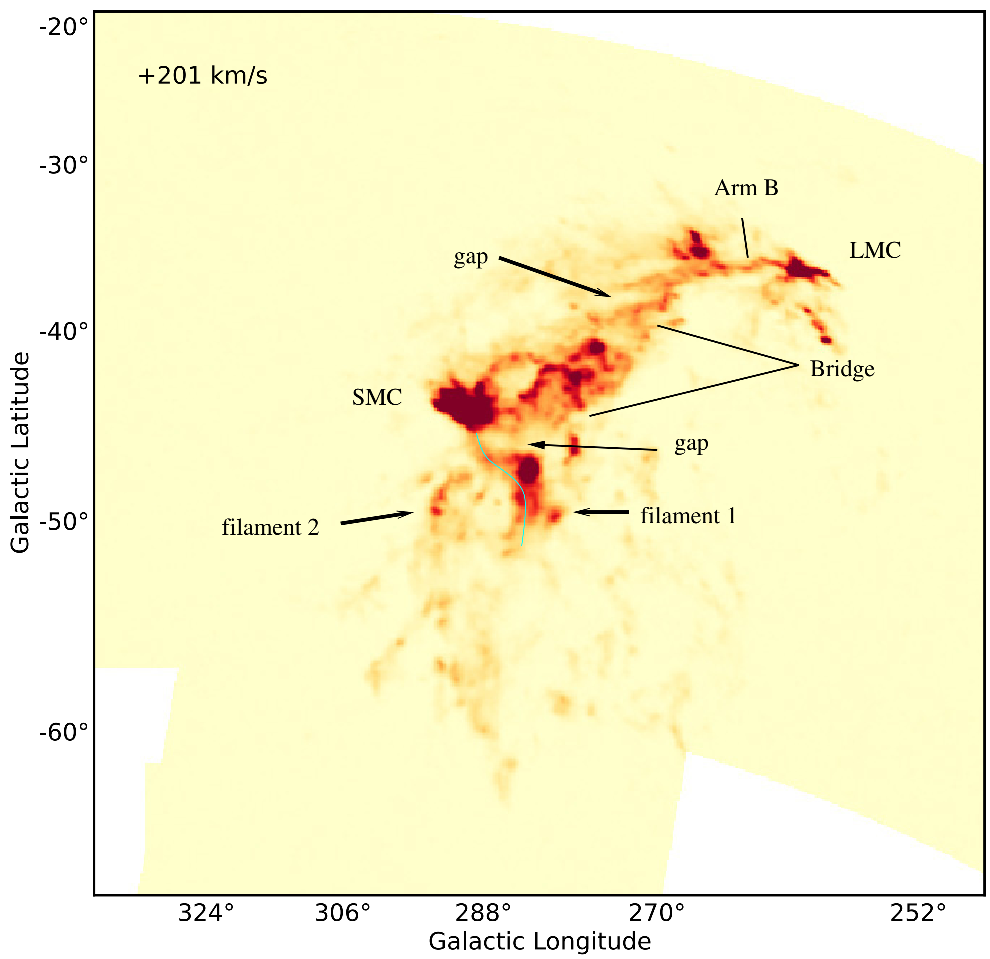

Figure 7. Channel map at +201 km s^{-1}. The Small Magellanic Cloud, Large Magellanic Cloud, Magellanic Bridge, the dual filaments at the head of the MS, and Arm B are labeled. The gaps show that filament 1 is not connected to the LMC. The cyan line marks the position of filament 1, which appears to be connected to the SMC both spatially and kinematically.

(A color version of this figure is available in the online journal.)

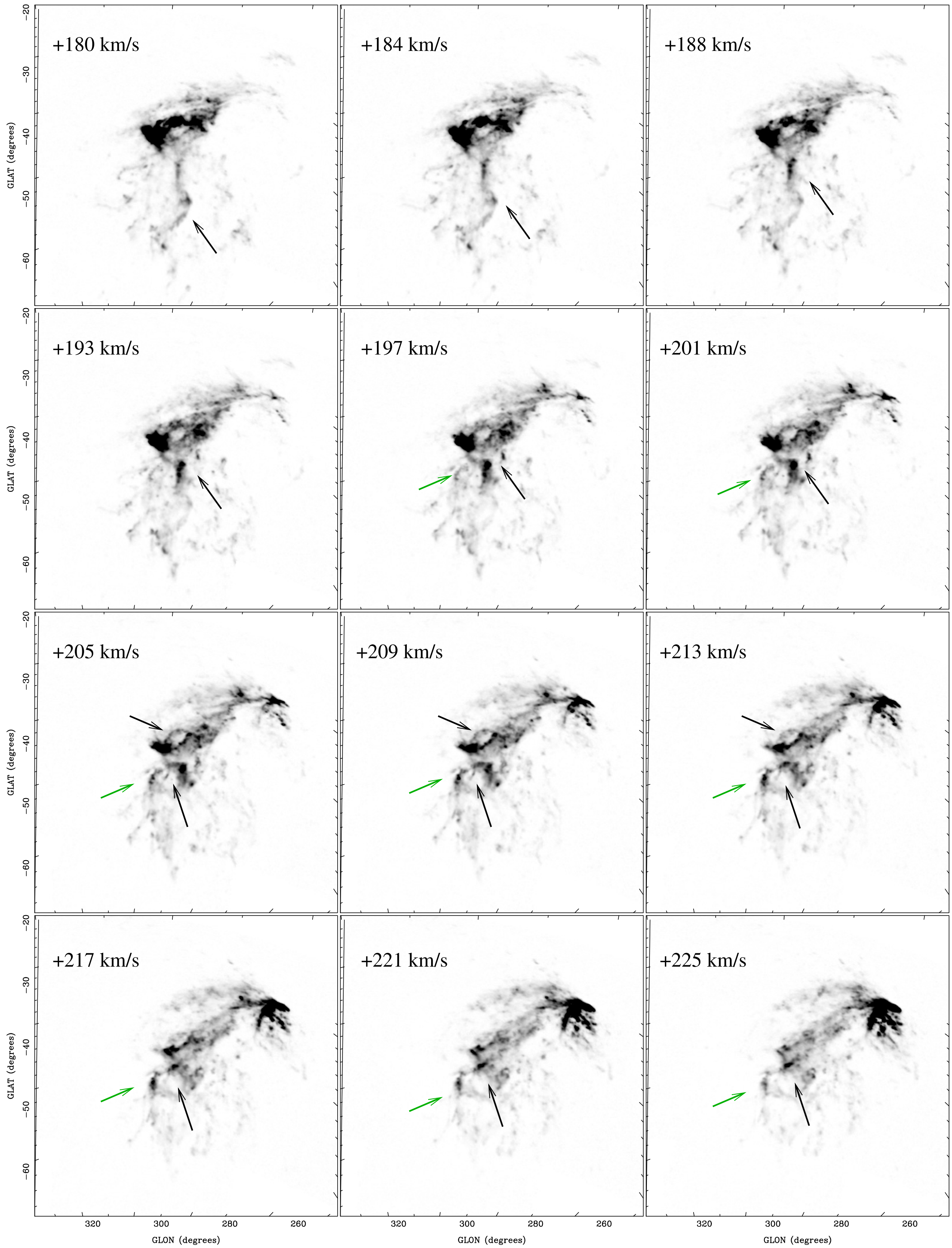

Figure 8. Channel maps of the GASS data cube from the LSR velocity of +180 km s^{-1} to +225 km s^{-1}. These maps cover the area where Small Magellanic Cloud, Large Magellanic Cloud, and the head of the MS are located. Black and green arrows indicate filaments 1 and 2, respectively.

(A color version of this figure is available in the online journal.)

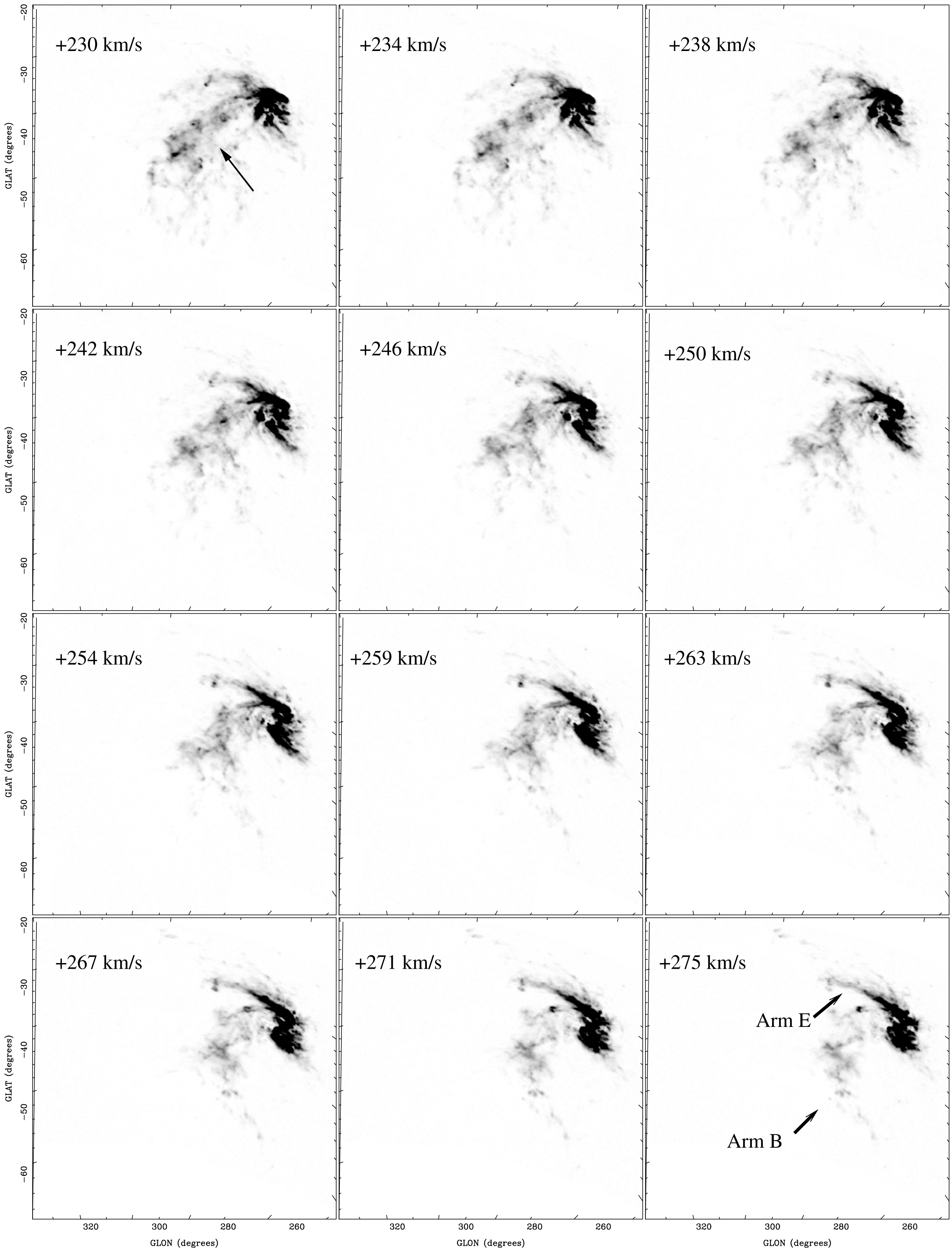

Figure 9. Same as Figure 8, except showing channel maps with LSR velocity from +230 km s^{-1} to +275 km s^{-1}. This velocity range is dominated by the H I gas from the LMC and Magellanic Bridge. The black arrow in the +230 km s^{-1} channel map indicates the location of the Magellanic Bridge where filament 1 is now mixed in. Arms E and B are labeled in the last channel map and a sinusoidal pattern is seen.

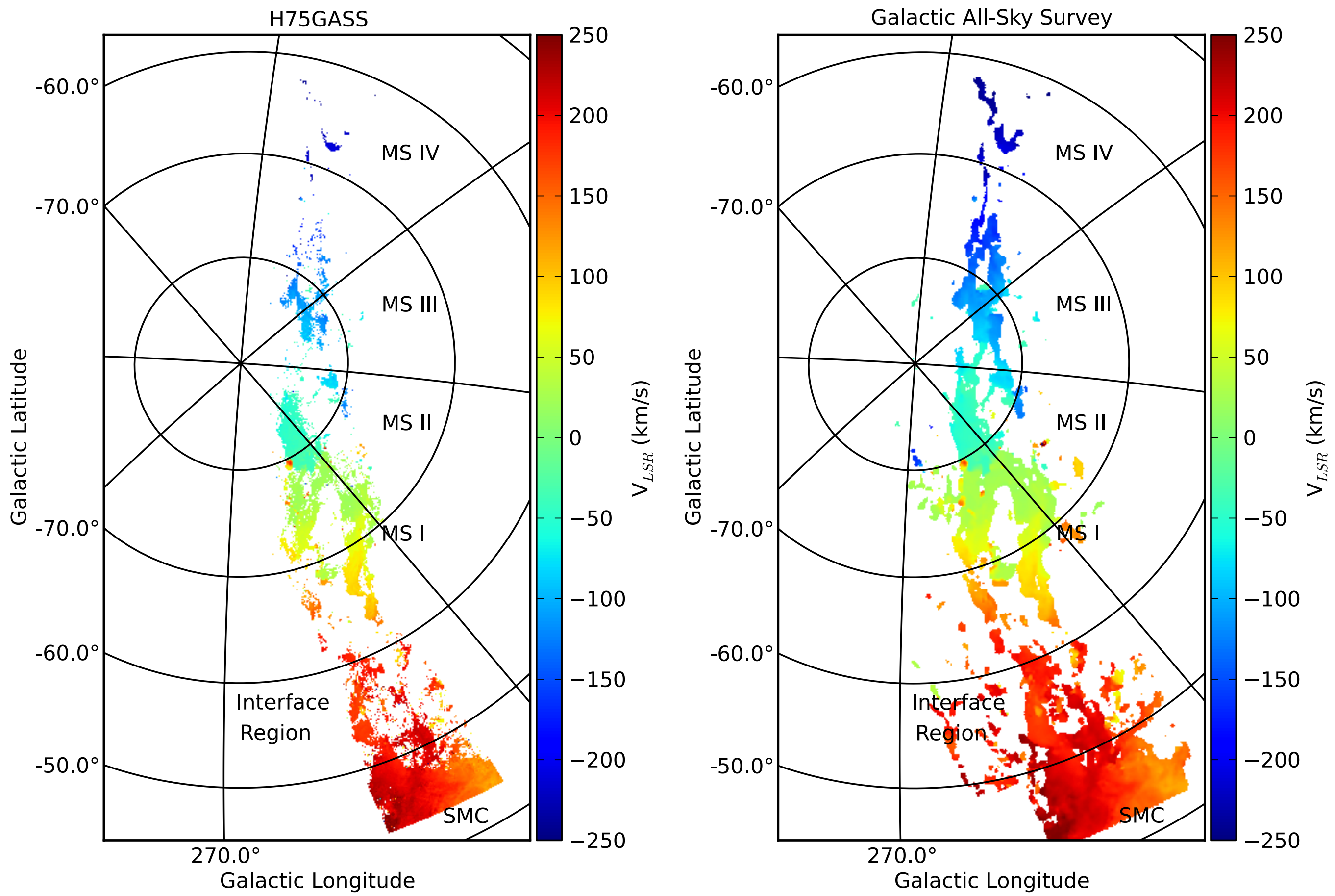

Figure 10. Velocity field map in the LSR frame with a velocity range from −250 to +250 km s^{-1} for H75GASS (left) and GASS (right). The Small Magellanic Cloud, the Interface Region, and MS I–IV are labeled.

(A color version of this figure is available in the online journal.)

a significant number of compact sources, which cannot be resolved in the lower resolution GASS and HIPASS data. This is clearly seen in the peak $N_{\rm H\,I}$ distribution (Figure 4). We show the velocity FWHM distribution of both catalogs in Figure 6. HVCs that overlap with the Galactic emission and/or lie at the spatial edge of the image and galaxies have been excluded in this plot. This figure shows that the excellent spectral resolution of GASS and H75GASS allows clouds with narrow-line components to be resolved. Most of the HVCs in our catalog and that of P02 have velocity FWHM of 15–25 km s^{-1} and 35–45 km s^{-1}, respectively. While few in number, our catalog does contain HVCs with large velocity FWHM (>40 km s^{-1}).

6. H I GAS AND KINEMATIC DISTRIBUTION

The MS has traditionally been viewed as consisting of six main concentrations (e.g., Mathewson et al. 1974). Subsequent observations with higher sensitivity revealed its complexity (see, e.g., Cohen 1982; Putman et al. 2003; Brüns et al. 2005; Nidever et al. 2008). Two distinct filaments were recovered, which run alongside each other with no clear starting point but appeared to be connected to the IFR (Brüns et al. 2005). Brüns et al. (2005) defined a separation between the IFR and the start of the MS near $l = 300°$ and $b = -61°$. Nidever et al. (2008) studied the MS and LA using a Gaussian decomposition method on the LAB data and claimed to trace one of the MS filaments back to the southeast H I overdensity region of the LMC. In this section, we use both the H75GASS and GASS data (complementary to each other) to revisit the overall morphology and kinematics of the MS, and to discuss the detailed morphology of filaments and HVCs in the MS.

6.1. *The Overall Morphology*

In Figures 1 and 2, we show the integrated H I column density maps of H75GASS and GASS data with nomenclature for various parts of the MS. In contrast to the study by Brüns et al. (2005), careful examination reveals that the two filaments of the MS are actually extended into the IFR, redefining the starting point of the MS. This continuity is also observed in the LAB data studied by Nidever et al. (2008). They showed that both filaments are running parallel at the head of the stream.

To trace the two filaments at the head of the stream, we use the GASS data, which has a better angular resolution than the LAB data. Figure 7 shows the area of investigation, which covers the SMC, LMC, and the head of the MS. The dual filaments are also labeled as filaments 1 and 2. A series of channel maps in the $V_{\rm LSR}$, ranging from +180 to +275 km s^{-1}with an interval of ∼4 km s^{-1}, are shown in Figures 8 and 9. Tracing the most prominent filament (namely filament 1, indicated by a black arrow) from velocity channels between +180 and +201 km s^{-1}, we find that it extends toward the SMC. A connection to the SMC emerges at +201 km s^{-1} and extends into the northern end of the Magellanic Bridge (the second black arrow as shown in the +205 km s^{-1} channel map), where H I gas from the SMC

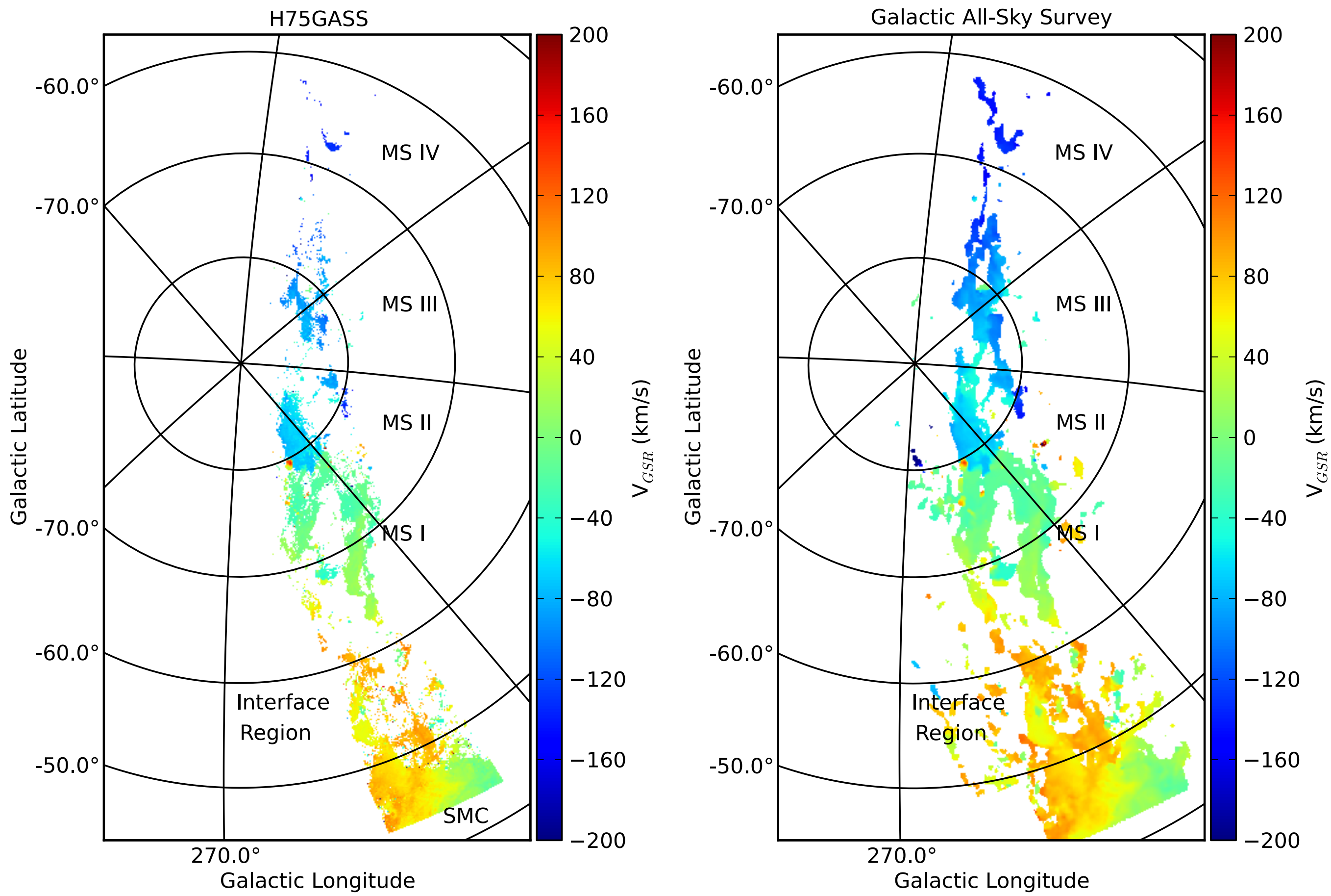

Figure 11. Same as Figure 10, except in the GSR velocity reference frame with a velocity range from −200 to +200 km s^{-1}.
(A color version of this figure is available in the online journal.)

is dominant. The exact ending point of filament 1 is ambiguous as it eventually mixes in with the Magellanic Bridge emission. In Figure 7, we show the channel map at +201 km s^{-1}in which distinct gaps are indicated. Gaps are common along the MS. Examining the channel maps beyond +255 km s^{-1}, we find that the gas from the LMC is dominant and eventually a distinct sinusoidal pattern emerges from the Arm B of LMC (see the last channel map of Figure 9). This gaseous feature appears isolated and does not seem to connect to filament 1. The exact starting point of filament 2 is hard to trace but the overall structure appears to be connected to the Magellanic Bridge through SMC (indicated by a green arrow).

These two filaments appear to be widely separated at the head of the stream and become thinner and have decreasing H I column density from the head to the tail of the stream. They eventually turn into a clumpy filamentary structure, which is not shown in this study but is revealed in the studies by Stanimirović et al. (2008) and Nidever et al. (2010). They also appear to be twisted several times along the stream in a double-helical structure (Putman et al. 2003).

We present the velocity field of the H75GASS and GASS data in $V_{\rm LSR}$ in Figure 10 and $V_{\rm GSR}$ in Figure 11. The maps show that the observed MS covers a large velocity range, $-250 \lesssim V_{\rm LSR} \lesssim +250$ km s^{-1} and $-200 \lesssim V_{\rm GSR} \lesssim +200$ km s^{-1}. Faint and thin filamentary structures are not visible in these maps due to noise clipping but are visible in the integrated H I column density maps (Figures 1 and 2). While it is hard to disentangle the bifurcated feature spatially in the integrated H I column density map, the velocity field map provides a powerful tool to trace the filaments. The head of the stream starts at positive velocity and trails at negative velocity. The transition between the positive and negative velocity occurs near $(L_{\rm MS}, B_{\rm MS}) = -50^\circ, 0^\circ$ (i.e., MS II). This part of the stream is difficult to analyze because it extends across 0 km s^{-1} and crosses in front of the Sculptor Group galaxies that have velocities ranging from 50 to 700 km s^{-1} (Putman et al. 2003). Contamination from the Galactic emission depends on the selected velocity channels (see Section 3.1).

While the velocity gradient is clearly seen along the stream, a $V_{\rm LSR} = 5.6$ km s^{-1}deg^{-1} transverse velocity gradient, in the sense that velocity decreases as a function of increasing declination, was pointed out near $L_{\rm MS} = -50^\circ$ in Cohen (1982). The exact gradient is difficult to measure using HIPASS due to low spectral resolution (Putman et al. 2003). Examining the high spectral resolution of GASS and H75GASS data, we do not find such a transverse velocity gradient in the specified region ($L_{\rm MS} \sim -50^\circ$). However, we should point out that the structure in this region is contaminated by the Galactic emission. Proper subtraction of the Galactic emission is needed to further investigate the existence of the transverse velocity gradient in this particular region. Nevertheless, if we examine the position–velocity map in declination of the entire observed MS (D. Matthews et al. 2014, in preparation), a transverse velocity gradient of 6.4 km s^{-1} deg^{-1} in the GSR velocity is evident.

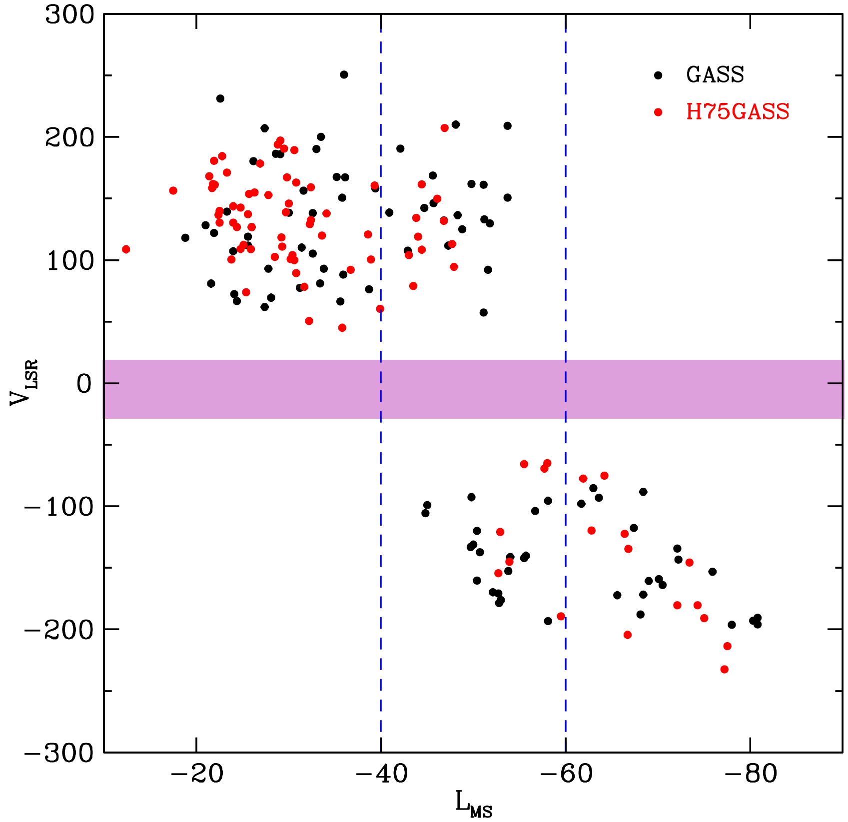

Figure 12. Distribution of clouds in L_{MS} vs. V_{LSR}. The dotted lines mark the south Galactic pole region. The black and red dots represent HVCs identified in GASS and H75GASS data cubes, respectively. Excluded from the plots are galaxies and HVCs that either overlap with the Galactic emission channels and/or lie at the spatial edge of the image. The shaded purple area marks the LSR velocity range from -30 km s^{-1} to +18 km s^{-1} that is dominated by the Galactic gas.

(A color version of this figure is available in the online journal.)

6.2. HVCs in the Magellanic Stream

We have shown the on-sky distribution of HVCs found in the region of the MS in Section 5.1 (see Figure 5). The most noticeable pattern is the overabundance of HVCs near the SGP (right panel of Figure 5). HVCs in this region partially overlap in V_{LSR} with the Sculptor Group of galaxies. The coincidence between these clouds and the Sculptor Group galaxies was first pointed out by Mathewson et al. (1975). Putman et al. (2003) carried out a comprehensive analysis and discussion regarding the origin of these clouds. Their conclusion is that these clouds are unlikely to be members of the Sculptor Group due to their velocity and spatial distributions not being much different from the bulk of Stream clouds.

Distinguishing between genuine HVCs associated with the MS and Sculptor Group is not easy based on the velocity information alone. Sculptor Group galaxies have a higher H I column density. However, HVCs in the MS are hard to distinguish from intrinsically large HVCs or tidal debris in the Sculptor Group if they exist. We find that HVCs with large differences in velocity and H I column density from the two filaments exist everywhere along the stream. Figure 12 shows the distribution of clouds in the L_{MS}–V_{LSR} plane. It shows that the overabundance of HVCs is not unique to the SGP. Large numbers of clouds are also found in the IFR ($L_{MS} \sim -20°$ to $-30°$). These were not seen by Putman et al. (2003) due to resolution and artifacts in the HIPASS data. Therefore, the overabundance of clouds in the SGP region is even less significant than before.

To probe the interaction between the MS and the ambient halo medium, it is useful to study the morphology of the HVCs. Here, we classify the HVCs in our catalog based on the morphological classification scheme of FSM13: (1) clouds with head–tail structure and velocity gradient (HT); (2) clouds with head–tail structure but without velocity gradient (:HT); (3) bow-shock shaped clouds (B); (4) symmetric clouds (S); and (5) irregular/complex clouds (IC).

Among these groups, head–tail clouds are particularly interesting because their compressed heads with diffuse tails provide direct evidence of gas being stripped from the main condensation due to interaction with the surrounding ambient gas. Besides the traditional cometary structure, head–tail clouds also come in many other varieties. For example, they may contain an additional clump of diffuse gas, or have a kink in the tail or velocity gradient that is generally associated with the H I column density gradient. It is also known that head–tail clouds with a velocity gradient consist of two subgroups: those with the velocity of the head either leading (pHT) or lagging (nHT) the tail (Putman et al. 2011; FSM13). We omit head–tail clouds that do not resemble the obvious cometary-like structure due to different viewing angles in this study (see, e.g., Plöckinger & Hensler 2012).

We find no obvious differences in the distributions among groups 1 and 2, and the subgroups of pHT and nHT, and hence, we analyze them altogether here. In Figure 13, we show the on-sky V_{LSR} distribution of head–tail clouds with and without velocity gradients in the region of the MS. Their distributions in L_{MS} and B_{MS} are shown in Figure 14. Head–tail clouds found in

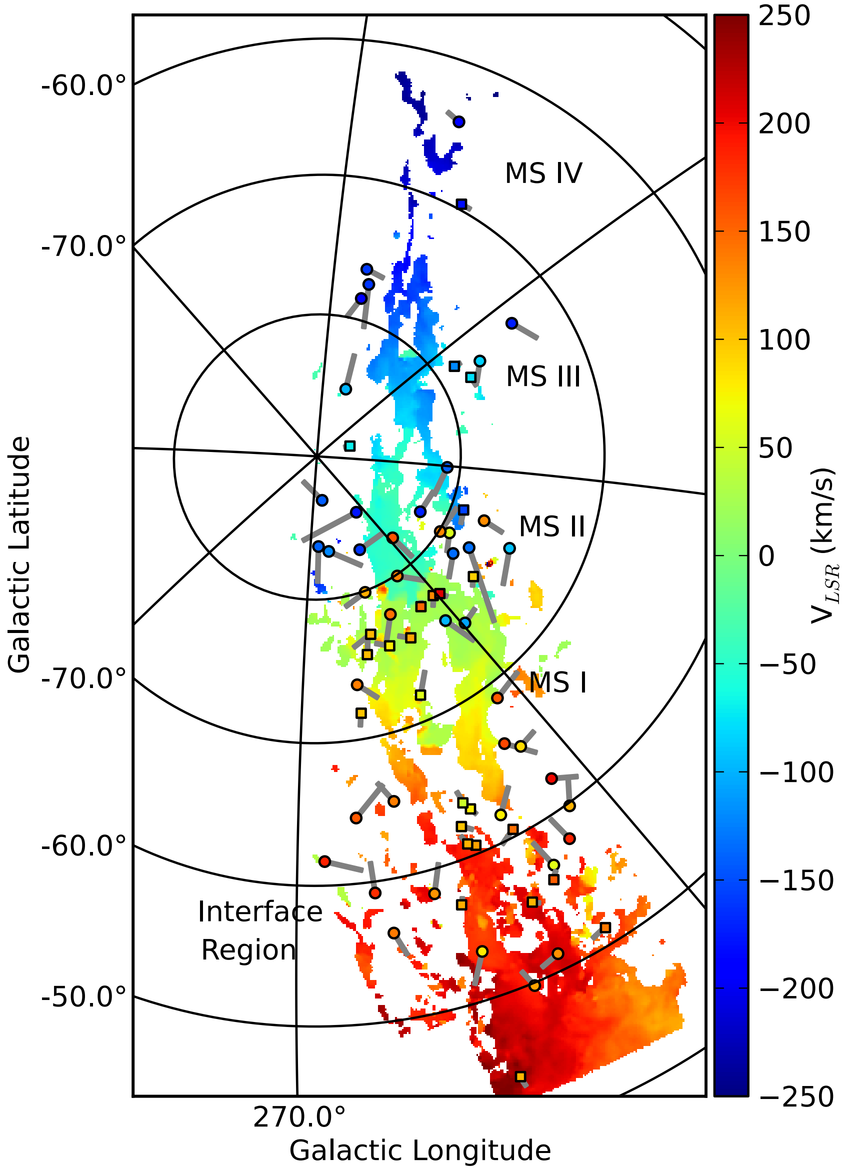

Figure 13. On-sky distribution of identified head–tail clouds in H75GASS (squares) and GASS (circles). The colors represent the LSR velocity of each head–tail cloud according to the color scale on the right side. The head and tail have been enlarged from their original size on the plot.

(A color version of this figure is available in the online journal.)

H75GASS data are generally compact and high in H I column density. For their distribution in $V_{\rm LSR}$, the head–tail clouds in general follow the velocity gradient along the stream. Few head–tail clouds have large $V_{\rm LSR}$ differences (100–200 km s^{-1}) from the $V_{\rm LSR}$ of the nearby filaments. This is most obvious near the SGP (or MS II) and IFR. Most head–tail clouds are at $-60^\circ \lesssim L_{\rm MS} \lesssim -20^\circ$ and $-5^\circ \lesssim B_{\rm MS} \lesssim +10^\circ$. Compared to the distribution of all HVCs in $B_{\rm MS}$ (Figure 4), most of the clouds at $B_{\rm MS} \sim 10^\circ$ are head–tail clouds.

The pointing direction of the head–tail clouds is also shown in Figure 13, with head and tail enlarged for better visibility. Due to the measurement errors in position angle, in some cases, we manually inspected the cloud and adjusted the values whenever necessary to better represent the pointing direction of the clouds (as discussed in FSM13). In Figure 15, we show the histogram of the pointing direction of the head–tail clouds. There is no preferential pointing direction, but careful examination reveals a nearly equal number pointing either toward (225°–315°) or away (45°–135°) from the head of the stream. We also find a total number of 70 head–tail clouds, which is ∼28% of all HVCs in our catalog. 60% (42/70) of the head–tail clouds show a clear velocity gradient, with a nearly equal number of clouds for the velocity gradient subgroups, i.e., 20 versus 21 for nHT and pHT, respectively. The percentages are very similar to those found in the LA region (FSM13). We have about a factor of six more head–tail clouds in this study than the study by Putman et al. (2011) in the same region. This may be due partly to different selection criteria. While the LA region still has a factor of 1.5 more head–tail clouds than the MS region, this finding is unexpected because disturbed clouds are absent in MS VI (Stanimirović et al. 2008). We will discuss the implication of the pointing direction and large number of head-tail clouds in the MS in Section 7.

The bow-shock-shaped clouds have a similar morphological structure to the head–tail clouds. They are characterized by a compressed head but with two deflected gas wings instead of a tail. Many studies suggest that bow-shock-shaped clouds are less common than head–tail clouds despite both of them

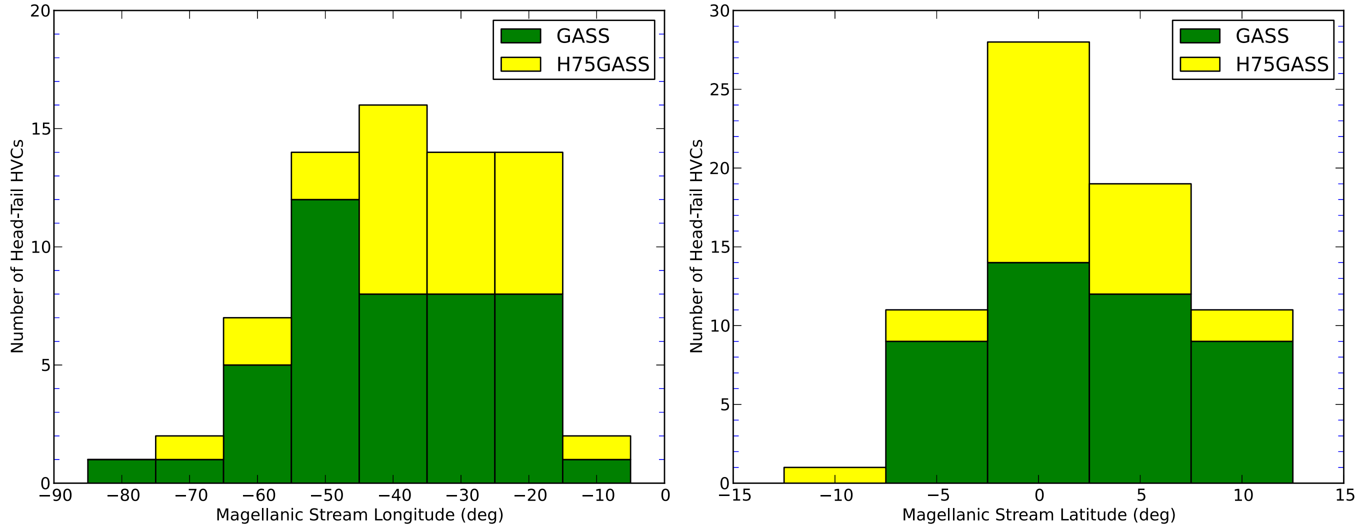

Figure 14. Histograms of head–tail clouds in L_{MS} and B_{MS}. The green and yellow represent head–tail clouds detected in GASS and H75GASS, respectively.

(A color version of this figure is available in the online journal.)

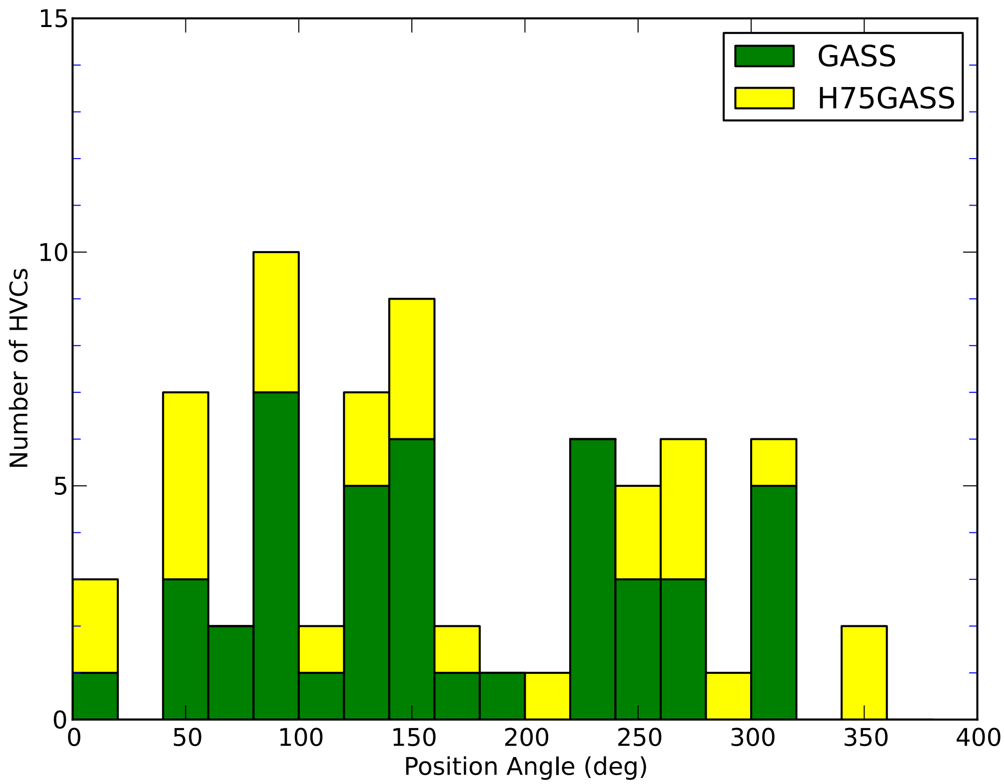

Figure 15. Histogram of position angles relative to the MS coordinates for all the head–tail clouds. 0° is parallel to the B_{MS} and the angle turns anticlockwise. 90° infers that the head of the cloud is pointed away from the general motion of the Magellanic System and parallel to the L_{MS}. The green and yellow represent head–tail clouds detected in GASS and H75GASS, respectively.

(A color version of this figure is available in the online journal.)

showing evidence of ram pressure interaction with the ambient medium (see, e.g., Westmeier et al. 2005; FSM13). On the other hand, symmetric clouds morphologically do not show signs of disturbance, although a head–tail cloud pointed directly along the line of sight can appear as a symmetric cloud. The total numbers of bow-shock-shaped and symmetric clouds are 8 and 35 in our catalog, respectively. This is about half the number of symmetric clouds in the MS as compared to the LA region. Figure 16 shows the distributions of bow-shock-shaped (diamonds and crosses) and symmetric clouds (hexagons and triangles) in V_{LSR}. Distributions of symmetric clouds in L_{MS} and B_{MS} are shown in Figure 17. They are distributed evenly across the entire range of L_{MS}, but mainly populate the range of ∼0°–5° in B_{MS}. The V_{LSR} distribution is quite similar to the one for head–tail clouds. Velocity gradients are common among the symmetric clouds. One notable, distinctive bow-shock-shaped cloud is HVC+73.7−67.5−213, which is located in MS IV. It is relatively large (1°.2) compared to others found in this study.

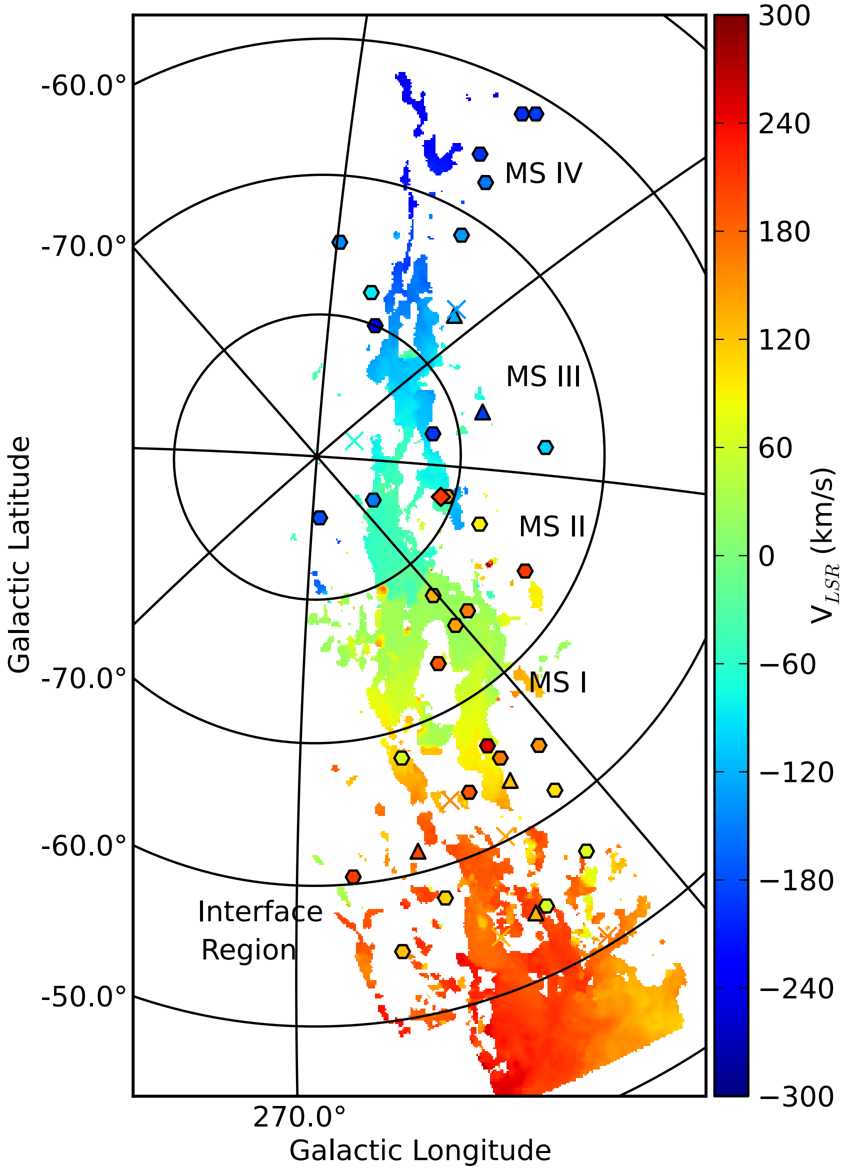

Figure 16. On-sky distribution of symmetric and bow-shock-shaped clouds. The colors represent the LSR velocity of each cloud according to the color scale on the right side. The diamonds and crosses represent the bow-shock-shaped clouds for the GASS and H75GASS data, respectively. The hexagons and triangles represent the symmetric clouds for the GASS and H75GASS data, respectively.

(A color version of this figure is available in the online journal.)

7. DISCUSSION

The formation of the MS has previously been attributed to either tidal or ram pressure mechanisms. Many efforts have been put into creating tidal models that accurately reproduce the global morphology such as the bifurcation of the MS. However, these tidal models fail to reproduce some of the observed features, such as the gradual decrease in H I column density along the stream. Ram pressure models, on the other hand, are able to help overcome this problem. Thus, the formation of the MS might be due to a combination of ram pressure and tidal stripping. Implementing both formation mechanisms simultaneously into simulations is not an easy task due to the large number of particles required to resolve the ISM and hot gas interaction. A notable attempt to employ both physical mechanisms is the study of Mastropietro et al. (2005). The drawback of their model is the sole consideration of two-body tidal interaction (MW–LMC), whereas in many tidal models, the SMC plays an important role in the formation of the MS. Metallicity measurements of *FUSE* and *HST* spectra suggest that most of the MS originates from the SMC (Sembach et al. 2001; Fox et al. 2010, 2013). In this section, we mainly discuss the effect of ram pressure stripping on the MS.

Aspects such as overall morphology and decrease in H I column density of the two filaments can be explained by the ram pressure model and evaporation of gas clouds. Models of ram pressure stripped galaxies (viewed edge-on) have shown that ram pressure is sufficient to remove part of the neutral gas from the disk (Mastropietro et al. 2005). The stripped gas trails behind the galaxy and the morphology at early times looks like a bow shock (see, e.g., Figure 4 of Mastropietro et al. 2005). As the interaction time continues, the gas in the disk decreases significantly. Eventually, islands of complex filaments are formed in the trailing direction and fan out near the end (Steinhauser et al. 2012), which is morphologically similar to the MS that we see today (Stanimirović et al. 2008). Clouds that

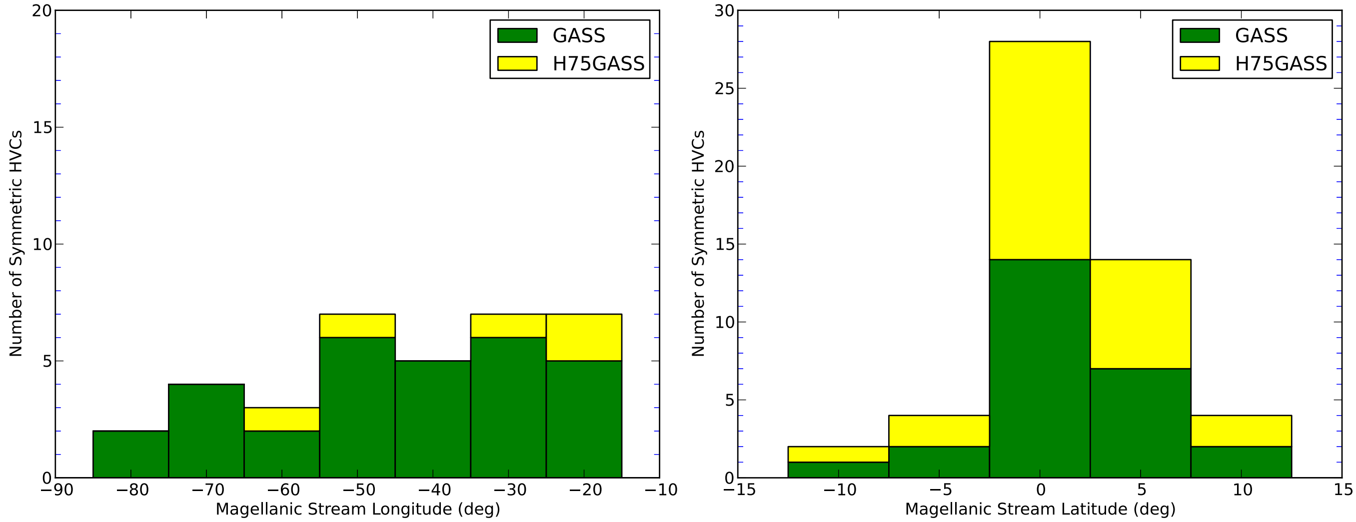

Figure 17. Same as Figure 14, but for symmetric clouds.

(A color version of this figure is available in the online journal.)

are stripped first would have longer interaction time with the hot halo and sustain a larger loss of gas due to evaporation.

To further investigate the effect of ram pressure on a smaller scale, we examine the distributions of head–tail clouds and their pointing directions. These head–tail clouds are presumably the debris of larger filaments broken off due to ram pressure stripping. Thus, they are expected to follow the motion of the larger filaments, i.e., with their head pointing toward the SMC and their tail pointing in the direction of decreasing $L_{\rm MS}$. However, they seem to be pointing in a random direction, similar to the finding in the LA region (FSM13). This is a rather surprising result because the random motion of head–tail clouds in the region of the LA is presumably caused by strong turbulence generated from the collision between the LA and the Galactic disk gas. This scenario of incoming warm neutral gas colliding with the hotter ambient medium (Audit & Hennebelle 2005) is inadequate to explain the random pointing of head–tail clouds in the MS region, even though turbulence must be at play as well. We look into the cascade scenario, which was originally proposed to explain the observed Hα emission along the MS (Bland-Hawthorn et al. 2007). In the hydrodynamical simulation of Bland-Hawthorn et al. (2007), the upstream clouds experience gas depletion via Kelvin–Helmholtz (KH) instability due to interaction with the hot halo. The depleted gas plows into the following cloud, which leads to shock ionization and depletion of the downstream clouds. The entire process continues downstream like a chain-reaction. During this process, the downstream clouds transfer momentum to the depleted gas in the front, which results in Rayleigh–Taylor (RT) instabilities. With both KH and RT instabilities, the process becomes highly turbulent for the entire region. This scenario agrees with the observational properties of head–tail clouds in the MS.

The lifetime of the disrupted clouds in the cascade scenario is 100–200 Myr, which is relatively short compared to the age of the stream (1–2 Gyr) as estimated from simulations. Constant replenishment of gas from the MCs is needed to reproduce the observed structure (Bland-Hawthorn et al. 2007). Other physical parameters can also lengthen the lifetime and govern the stability of clouds, for example, magnetic field, dark-matter, heat conduction, size, and halo and cloud densities. Two- and/or three-dimensional hydrodynamical simulations have experimented with these parameters (see, e.g., Quilis & Moore 2001; Plöckinger & Hensler 2012; Heitsch & Putman 2009; Vieser & Hensler 2007).

In Quilis & Moore (2001), the behavior of pure gas clouds and dark-matter dominated HVCs interacting with the different halo environment was investigated. They found that head–tail structures emerge when the ambient environment reaches a density of 10^{-4} cm^{-3} with a cloud velocity of 200 km s^{-1}. HVCs with a dark matter component survive longer (∼10 Gyr) as compared to those without (∼10 Myr). However, the same cloud was not tested both with and without dark matter. The recent Plöckinger & Hensler (2012) models considered this effect and found that dark matter free HVCs can easily survive for 100 Myr. Their model also suggests that dark matter free clouds are physically much similar to the observed large HVC complexes with a heterogeneous multi-phase internal gas structure.

The effect of heat conduction for stabilizing the HVCs (or Giant Molecular Clouds) is explored by Vieser & Hensler (2007). Their models show that clouds with two-phase structures can stabilize and survive longer as a result of heat conduction. While heat conduction may explain the longer survival timescale of head–tail clouds in the MS, massive clouds like the filaments of the MS have yet to be tested in simulations (G. Hensler 2014, private communication). Heitsch & Putman (2009) also explored effects of various physical parameters based on two experimental setups: wind-tunnel and free-fall. Their results show that clouds with H I masses less than $10^{4.5}$ $M_\odot$ will lose their gas after moving only 10 kpc or less under typical halo density and relative velocity conditions. The visibility of the head–tail structure depends on the viewing angle. Nevertheless, all the hydrodynamical simulations have so far only considered clouds at lower z (distance from the Galactic plane) due to the large uncertainty in the halo density beyond 10 kpc. This implies that these models might not be suitable for explaining the evolution of HVCs originating from the MCs. Interestingly, HVCs created with these models are morphologically and physically similar to what we observe, e.g., the bow-shock-shaped cloud, HVC+73.7−67.5−213, and the head–tail clouds.

There is an overall larger number of head–tail clouds in the MS region found in this study compared to the study by Putman et al. (2011) (see Section 6.2). It is possible that we missed some of the head–tail clouds not resembling classical head–tail morphologies due to different viewing angles (see Plöckinger & Hensler 2012), which would increase the number of head–tail clouds. While a larger number of head–tail clouds is found, there is a significant decrease in number toward the tail end ($L_{MS} > -60°$; see the left panel of Figure 14). This is consistent with the finding of a lack of head–tail clouds in the region of MS IV (Stanimirović et al. 2008), which suggests that ram pressure stripping has less of an effect on the tail end of the stream. This is not surprising given that the predicted model distance is the largest at the tail end of the stream, which the ram pressure decreases as a function of distance square in an assumed isothermal halo model. It is also possible that the tail of the MS is radially aligned along the line of sight (see Figure 4 of Diaz & Bekki 2012), in which case viewing geometry would reveal more symmetric cloud shapes.

We find that the number of symmetric clouds is about a factor of two smaller than the number of head–tail clouds in the range $-60° < L_{MS} < -20°$. A slight increase in the number of symmetric clouds as compared to head–tail clouds is observed beyond $L_{MS} \sim -60°$. We know that the MS VI region is exclusively populated with symmetric clouds (Stanimirović et al. 2008). This raises the question of whether we will see a continual trend of increasing numbers of symmetric clouds in the MS V region, which is outside our currently studied area. If the answer is yes, then this would further confirm the model prediction of distance increasing as a function of L_{MS}. With this in mind, it is rather puzzling to see that the northern extension of the stream (Nidever et al. 2010) has a very different morphology from other parts of the MS. Morphologically, it looks more like the LA (FSM13). A statistical analysis of different morphological types of HVCs in the northern extension might shed some light on the distance scale of the farthest end of the stream.

8. SUMMARY AND CONCLUSIONS

We have compiled a catalog of HVCs in the MS using new ATCA and Parkes (GASS) data. The catalog includes 251 HVCs and two galaxies. Most of the clouds detected in the combined H75GASS are unique. We used *Duchamp* as a source finding tool and to parameterize the detected sources. Most of the parameters were derived from *Duchamp* except the angular size and the peak H i column density, which were independently determined. We made a comparison between our catalog and Putman et al. (2002), who employed the reprocessed HIPASS data for their study.

We have presented the distributions of clouds and their properties. The HVCs agglomerate in a narrow MS latitude (B_{MS}) range of $\pm 10°$ and decrease linearly with decreasing MS longitude (L_{MS}). The kinematics show bimodality in V_{LSR} but none in V_{GSR}. The majority of the clouds detected in GASS have lower H i column densities than those in H75GASS. The overall velocity FWHM distribution is similar to that found in the LA region (FSM13).

The overall morphology and kinematics of the MS have been revisited. We find that the two filaments of the MS are extended into the IFR, connected to the SMC, and extend into the northern end of the Magellanic Bridge. The former finding is consistent with the study by Nidever et al. (2008), but differs from the conclusion of Brüns et al. (2005). The connection to the SMC and Magellanic Bridge is contradictory to the conclusions of Nidever et al. (2008). Our suggestion that the two filaments of the MS are twisted and largely emanate from the SMC is consistent with the Fox et al. (2013) metallicity measurements, which show 0.1 solar metallicity along much of the Stream. While we could not investigate the existence of the transverse velocity gradient as seen in Cohen (1982), in this study, we found a clear transverse velocity gradient of 6.4 km $s^{-1}deg^{-1}$ in the GSR velocity frame based on the position–velocity map of D. Matthews et al. (2014, in preparation).

We find that the MS has a complex filamentary structure. Morphological classification is presented and distributions of each type are discussed. In contrast to the studies by Stanimirović et al. (2008) and Putman et al. (2011), we found a large number of head–tail clouds in the MS region. This strongly suggests that ram pressure stripping plays an important role in the formation mechanism of the MS. The pointing direction of the head–tail clouds appear to be random, which suggests the presence of strong turbulence. The turbulence induced by the cascade scenario is a likely cause. We also discussed various physical parameters that can lengthen the lifetime of the HVCs. While hydrodynamical simulations of HVC may not explain the HVCs origin from the MCs, they do show how small-scale structures may arise. The evaporation of gas clouds is also responsible for the decrease in H i column density as seen toward the tail end of the MS.

B.Q.F. is the recipient of a John Stocker Postdoctoral Fellowship from the Science and Industry Research Fund. This research made use of APLpy, an open-source plotting package for Python, hosted at http://aplpy.github.com. This publication also made use of data products from Parkes and Narrabri radio telescopes. The Australia Telescope Compact Array/Parkes radio telescope is part of the Australia Telescope National Facility, which is funded by the Commonwealth of Australia for operation as a National Facility managed by CSIRO. We thank Kenji Bekki and Cameron Yozin for generating fruitful discussion, Tobias Westmeier for providing his parameterization code and helpful comments, and Matthew Whiting for assisting with the running of *Duchamp* on large data cubes.

REFERENCES

Audit, E., & Hennebelle, P. 2005, A&A, 433, 1
Barnes, D. G., Staveley-Smith, L., de Blok, W. J. G., et al. 2001, MNRAS, 322, 486
Besla, G., Kallivayalil, N., Hernquist, L., et al. 2007, ApJ, 668, 949
Besla, G., Kallivayalil, N., Hernquist, L., et al. 2012, MNRAS, 421, 2109
Bland-Hawthorn, J., Sutherland, R., Agertz, O., & Moore, B. 2007, ApJL, 670, L109
Braun, R., & Burton, W. B. 1999, A&A, 341, 437
Brüns, C., Kerp, J., Staveley-Smith, L., et al. 2005, A&A, 432, 45
Cohen, R. J. 1982, MNRAS, 199, 281
Connors, T. W., Kawata, D., & Gibson, B. K. 2006, MNRAS, 371, 108
de Heij, V., Braun, R., & Burton, W. B. 2002, A&A, 391, 159
Diaz, J., & Bekki, K. 2011, PASA, 28, 117
Diaz, J. D., & Bekki, K. 2012, ApJ, 750, 36
For, B.-Q., Staveley-Smith, L., & McClure-Griffiths, N. M. 2013, ApJ, 764, 74
Fox, A. J., Richter, P., Wakker, B. P., et al. 2013, ApJ, 772, 110
Fox, A. J., Wakker, B. P., Smoker, J. V., et al. 2010, ApJ, 718, 1046
Gardiner, L. T., & Noguchi, M. 1996, MNRAS, 278, 191
Gibson, B. K., Giroux, M. L., Penton, S. V., et al. 2000, AJ, 120, 1830
Heitsch, F., & Putman, M. E. 2009, ApJ, 698, 1485
Kalberla, P. M. W., Burton, W. B., Hartmann, D., et al. 2005, A&A, 440, 775
Kalberla, P. M. W., McClure-Griffiths, N. M., Pisano, D. J., et al. 2010, A&A, 521, A17
Kallivayalil, N., van der Marel, R. P., & Alcock, C. 2006a, ApJ, 652, 1213
Kallivayalil, N., van der Marel, R. P., Alcock, C., et al. 2006b, ApJ, 638, 772
Kallivayalil, N., van der Marel, R. P., Besla, G., Anderson, J., & Alcock, C. 2013, ApJ, 764, 161
Lu, L., Sargent, W. L. W., Savage, B. D., et al. 1998, AJ, 115, 162

Lu, L., Savage, B. D., & Sembach, K. R. 1994, ApJL, 437, L119
Mastropietro, C., Moore, B., Mayer, L., Wadsley, J., & Stadel, J. 2005, MNRAS, 363, 509
Mathewson, D. S., Cleary, M. N., & Murray, J. D. 1974, ApJ, 190, 291
Mathewson, D. S., Cleary, M. N., & Murray, J. D. 1975, ApJL, 195, L97
McClure-Griffiths, N. M., Pisano, D. J., Calabretta, M. R., et al. 2009, ApJS, 181, 398
McGee, R. X., & Newton, L. M. 1986, PASAu, 6, 471
Moore, B., & Davis, M. 1994, MNRAS, 270, 209
Nidever, D. L., Majewski, S. R., & Burton, W. B. 2008, ApJ, 679, 432
Nidever, D. L., Majewski, S. R., Butler Burton, W., & Nigra, L. 2010, ApJ, 723, 1618
Plöckinger, S., & Hensler, G. 2012, A&A, 547, A43
Putman, M. E., de Heij, V., Staveley-Smith, L., et al. 2002, AJ, 123, 873
Putman, M. E., Gibson, B. K., Staveley-Smith, L., et al. 1998, Natur, 394, 752
Putman, M. E., Saul, D. R., & Mets, E. 2011, MNRAS, 418, 1575
Putman, M. E., Staveley-Smith, L., Freeman, K. C., Gibson, B. K., & Barnes, D. G. 2003, ApJ, 586, 170
Quilis, V., & Moore, B. 2001, ApJL, 555, L95
Richter, P., Fox, A. J., Wakker, B. P., et al. 2013, ApJ, 772, 111
Sembach, K. R., Howk, J. C., Savage, B. D., & Shull, J. M. 2001, AJ, 121, 992
Shattow, G., & Loeb, A. 2009, MNRAS, 392, L21
Stanimirović, S., Hoffman, S., Heiles, C., et al. 2008, ApJ, 680, 276
Staveley-Smith, L., Kim, S., Calabretta, M. R., Haynes, R. F., & Kesteven, M. J. 2003, MNRAS, 339, 87
Steinhauser, D., Haider, M., Kapferer, W., & Schindler, S. 2012, A&A, 544, A54
van der Marel, R. P., Alves, D. R., Hardy, E., & Suntzeff, N. B. 2002, AJ, 124, 2639
Venzmer, M. S., Kerp, J., & Kalberla, P. M. W. 2012, A&A, 547, A12
Vieser, W., & Hensler, G. 2007, A&A, 472, 141
Wakker, B. P. 1991, A&A, 250, 499
Wakker, B. P. 2001, ApJS, 136, 463
Wannier, P., & Wrixon, G. T. 1972, ApJL, 173, L119
Westmeier, T., Brüns, C., & Kerp, J. 2005, A&A, 432, 937
Westmeier, T., & Koribalski, B. S. 2008, MNRAS, 388, L29
Westmeier, T., Popping, A., & Serra, P. 2012, PASA, 29, 276
Whiting, M. T. 2012, MNRAS, 421, 3242